A dual interpolation boundary face method for three-dimensional potential problems

Jianming Zhang*, Baotao Chi, Weicheng Lin, Chuanming Ju

State Key Laboratory of Advanced Design and Manufacturing for Vehicle Body, College of Mechanical and Vehicle Engineering, Hunan University, Changsha 410082, China

*****Correspondence to: Jianming Zhang

College of Mechanical and Vehicle Engineering, Hunan University, Changsha 410082, China

Telephone: +86-731-88823061

E-mail: zhangjm@hnu.edu.cn

Abstract

A dual interpolation boundary face method (DiBFM) is presented for solving three-dimensional potential problems. The DiBFM is an alternative implementation of the boundary face method (BFM) and inherits all the merits of BFM, which has been proposed to unify the continuous and discontinuous elements, improve the accuracy of the interpolation calculation and alleviate the heavy task of mesh generation. The DiBFM implementation is based on a new type of elements, called the dual interpolation elements, in which the nodes are classified into virtual nodes and source nodes. Despite the introduction of virtual nodes in the dual interpolation elements, only source nodes of each element are taken as the collocation points. Corresponding constraint equations using the MLS approximation are formulated to condense the degrees of freedom for all virtual nodes, which does not result in the scale of final linear system increasing. In addition, even with some irregular elements in numerical simulation, accurate results and high convergence rates can be achieved by the DiBFM. The DiBFM is flexible and convenient to handle more complicated, real world structures without any geometric simplification in a fully automated manner. Numerical results have demonstrated the validity, high accuracy and superior convergence of the proposed method.

Key words: potential problems; Dual interpolation; boundary face method; boundary element method; moving least-squares approximation.

1. Introduction

Boundary integral formulations [1] are attractive computational techniques for linear and exterior problems as they can reduce the dimensionality of the original problem by one. With the distinct

feature that only the boundary of the problem is required to be discretized into elements, the boundary element method (BEM) has been developed rapidly to such a level that it has been widely applied to solve very complicated engineering problems, such as potential problems [2-4], elastostatic problems [5], contact problems [6,7], fracture mechanics problems [8-10] and acoustics problems [11,12]. Since only the surface requires discretization in BEM, the mesh generation process is not as intensive compared to the finite element method (FEM). Note that the trial functions are required to maintain at least C^0 continuity as well as the connectivity requirements of the resulting mesh in FEM, which is not required for the BEM. One of the remarkable features between BEM and FEM is that both continuous and discontinuous elements can be applied in BEM. In addition, a key difficulty in FEM is to achieve the connectivity requirements of the desirable mesh [13], such as all-hexahedral mesh, which causes a large amount of work for automatic meshing. And for complex geometries, mesh generation can still be a bottleneck in BEM.

Meshless methods [14] were born with the objective of eliminating part of the difficulties associated with reliance on a mesh to construct the approximation. In recent years, a few different meshless boundary type meshless techniques combined with boundary integral equations (BIEs) have been developed and achieved remarkable progress in BEM, such as the hybrid boundary node method (HBNM) [15], the regular hybrid boundary node method (RHBNM) [16], the backward substitution method (BSM) [17]. the novel singular boundary method (NSBM) [18], the localized radial basis function collocation method (LRBFCM) [19], and so forth. The FEM also has made great achievements in practical application, but some limitations or drawbacks still exist in the conventional FEM formulation. In the efforts to improve the performance of standard FEM, the smoothed finite element method (S-FEM) has effectively addresses the weaknesses of FEM through the use of some meshfree concepts and techniques. To deal with the locking phenomena in FEM, various successful locking free methods have been developed and implemented. The edge-based smoothed finite element methods (ES-FEM) with a phantom-node method [20] has been successfully implemented in 2D linear elastic fracture mechanics. Nguyen-Xuan et al. [21] proposed a bubble enriched smoothed finite element method called the bES-FEM in 2D and bFS-FEM in 3D, which contribute to soften the bilinear form allowing the weakened weak (W^2) form to yield more accurate simulation results. Strain smoothing approaches were developed to avoid volumetric locking for

compressible or nearly incompressible linear elasticity problems [22]. Recently, Natarajan et al. [23] illustrated the connection between the virtual element method and the S-FEM theoretically and numerically. A linear smoothing scheme for linear and quadratic arbitrary convex polytopes was presented in detail [24]. S. Chakraborty et al. [25] proposed an optimal numerical integration scheme to improve the accuracy and convergence of a family of polygonal finite elements with Schwarz–Christoffel conformal mapping.

Various numerical methods to establish a natural link between CAD and CAE based on boundary representations have always been attracted much attention in BEM and FEM, such as the geometry-independent field approximation (GIFT) [26], the scaled boundary finite element method (SBFEM) [27] and the isogeometric boundary element method (IGASBFEM) [28]. The GIFT is a generalisation of isogeometric analysis (IGA), which allows adaptive local refinement of the solution field and establishes a tight integration between CAD and the CAE analysis. In the conventional IGA, the surfaces/volumes are represented by the tensor product structure of the NURBS. This requires the domain to be discretized with standard shapes and leads to a restricted number of boundary curves/surfaces. Also, this leads to excessive overhead of control points with refinement [28]. In the GIFT implementation, the geometry parameterization and solution approximation are based on the same shape functions spaces of NURBS, PHT-splines, and B-splines. The SBFEM is a novel semi-analytical technique, combining the advantages of the BEM and the FEM with unique properties of its own. It is worth mentioning that the SBFEM is implemented by the scaled boundary coordinate system; that is, the geometry of the domain should be transformed from the Cartesian coordinates to the scaled boundary coordinates, viz., circumferential and radial direction. Combined with IGA, a novel method named the IGASBFEM is developed within the framework of the SBFEM, which is employed the NURBS basis functions to approximate the unknown felds in the circumferential direction.

Taking the two basic ways of the BEM implementation, i.e. using continuous and discontinuous elements, we first discuss the benefits and drawbacks of these two type elements [29,30]. The first way is using the continuous elements, in which the collocation nodes coincide with the geometric vertices of elements. In terms of the properties of the shape functions of continuous elements, the interelement continuity of field variables and the continuity of the fields between the elements can be basically ensured. Nevertheless, it is tricky for the standard continuous elements to handle the corner

problems [31]. Besides, the continuous elements cannot meet the requirements of continuity and differentiability at the source node, which is not suitable for evaluation of the hypersingular integrals [32]. With the discontinuous elements, it is able to overcome the above weakness of continuous elements naturally. Beyond that, discontinuous elements have some other attractive advantages, including the simplification in the assembly and solution of the system matrix and greatly alleviating he heavy task of mesh generation. But in comparison with the continuous elements, the degrees of freedom increases rapidly when using the discontinuous elements with the same accuracy, which means much more computer resources are required. How to take full advantages of continuous and discontinuous elements has been a long-standing debate in the BEM community.

The dual interpolation boundary face method (DiBFM) [33] is an alternative implementation of the boundary face method (BFM) [34] and inherits all the merits of BFM, which has been proposed to unify the continuous and discontinuous elements, improve the accuracy of the interpolation calculation and alleviate the heavy task of mesh generation. The DiBFM has been successfully applied to elastostatic problems [35], contact problems [36] in two dimensions. The DiBFM implementation is based on a new type of elements, called the dual interpolation elements, in which the nodes are classified into virtual nodes and source nodes. Despite the introduction of virtual nodes, only source nodes of each element are taken as the collocation points. Corresponding constraint equations using the MLS approximation [37] are formulated to condense the degrees of freedom for all virtual nodes, which does not result in the scale of final linear system increasing. In addition, the geometry representation of the boundary faces of domain is exactly the same as the original B-rep data structure in standard solid modeling packages. Both the MLS approximation and boundary integration are performed in the parametric spaces of the faces. The geometric variables for the DiBFM implementation, such as out normal, Jacobians and etc, are implemented directly on the original CAD model rather than an elaborately built discretized model, which is different from the real model not only in geometry and topology, but also in representation data structure. Thus, a truly seamless interaction between CAD and CAE can be successfully achieved.

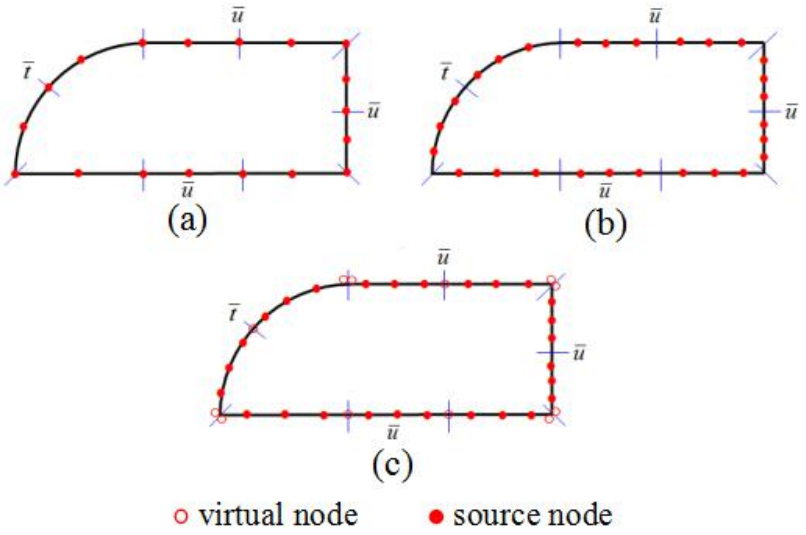

Fig. 1. Boundary discretization using quadratic elements: (a) continuous elements, (b) discontinuous elements, (c) dual interpolation elements.

An important topic in the computational field of BEM and FEM is to reduce the sensitivity of analysis results to the mesh distortions. Distorted meshes are often unavoidable in automatic mesh generation for complex geometries, which may produce discretizations with inferior approximation properties. An immediate consequence of mesh distortion is leading to inaccurate or even invalid computational analyses. Even with some distorted elements in numerical analysis, the DiBFM exhibits high performance of accuracy and convergence. Another attractive key innovation of the DiBFM is the alleviation of heavy task of mesh generation. A broad consensus has emerged that in the specific domain of high performance computing, automatic mesh generation is very difficult and time consuming for complex geometries. With the distinct property that both continuous and discontinuous elements can be applied in BFM, the DiBFM is a special and efficient method for solving three-dimensional (3-D) problems through the use of discontinuous grids. In order to meet the connectivity requirements of the resulting mesh in FEM, many researchers have done a great deal of work to deal with the disgusting hanging points in mesh generation, such as the grid-based method, octree-based algorithm, meshing techniques of splitting or insertion, and etc [38]. However, the undesirable effect of hanging points can be avoided by the DiBFM implementation. Discontinuous grids also can provide more convenience for mesh generation without considering the hanging points for its simplicity in dealing with complex geometries. This is a potential advantage of the DiBFM in the future work.

This paper is organized as follows. Section 2 describes the parameter mapping scheme based on

the surface element for 3-D problems. Detailed description of the dual interpolation method for 3-D potential problems is presented in Section 3. Section 4 demonstrates the governing equations, the boundary integral formulations of the DiBFM for 3-D potential problems. Numerical examples for 3-D potential problems are given in Section 5. Section 6 summarizes.

2. The approximation scheme in parametric space

One of the distinguishing features between DiBFM and BEM is that physical variables are implemented directly on the bounding surfaces rather than from elements in DiBFM. Both the dual interpolation and boundary integration in the DiBFM implementation are performed in the parameter space of each surface.

And a surface has a parametric representation of the form

$$\mathbf{r}(x,y,z)=\mathbf{r}(x(u,v),y(u,v),z(u,v))=\mathbf{r}(u,v) \tag{1}$$

where $\mathbf{r}$ is the position vector, u , v are the parametric coordinates of each surface. It is assumed that $\tilde{S}$, S denote the surface in parametric and Euclidean space, respectively, and a geometric map $F:\tilde{S}\to S$ can be created. Based on the geometric map F , the shape functions are constructed in the parameter space $\tilde{S}$.

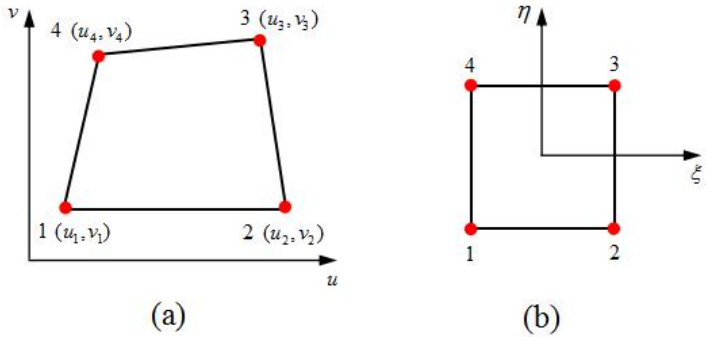

Fig.2. Four-node surface element: (a) quadrilateral element in parameter space and (b) coordinate mapping.

To illustrate the approximation scheme, a graphical illustration of the linear quadrilateral element in the parameter space $\tilde{S}$ for approximation is presented in Fig.2. Corresponding interpolation functions of each node for the linear quadrilateral element are given by

$$\begin{aligned} &N_1=\frac{1}{4}(1-\xi)(1-\eta),\quad N_2=\frac{1}{4}(1+\xi)(1-\eta),\\ &N_3=\frac{1}{4}(1+\xi)(1+\eta),\quad N_4=\frac{1}{4}(1-\xi)(1+\eta) \end{aligned} \qquad \xi,\eta\in[-1,1] \tag{2}$$

Considering the linear quadrilateral element, the coordinates (u,v) defined on the parameter space of each surface are interpolated by Eq. (3). The subsequent geometric data in Euclidean space at (u,v) can be calculated directly from the bounding surfaces, which makes a truly seamless interaction between CAD and CAE successfully achieved without any geometric simplification.

$$u=\sum_{i=1}^{4}N_i u_i,\quad v=\sum_{i=1}^{4}N_i v_i \tag{3}$$

where (ξ,η) is the usual local parametric coordinate defined on the quadrilateral surface element, (u_i,v_i) denotes the parametric coordinates of each node of the element.

3. Dual interpolation method for potential problems

This section introduces the details of the dual interpolation method for 3-D potential problems. The notion of dual interpolation elements in the DiBFM is introduced in Section 3.1. This concept is used in the first-layer interpolation to interpolate the physical variables in Section 3.2 and in the second-layer interpolation to condense the degrees of freedom of virtual nodes in Section 3.3.

3.1 Dual interpolation element

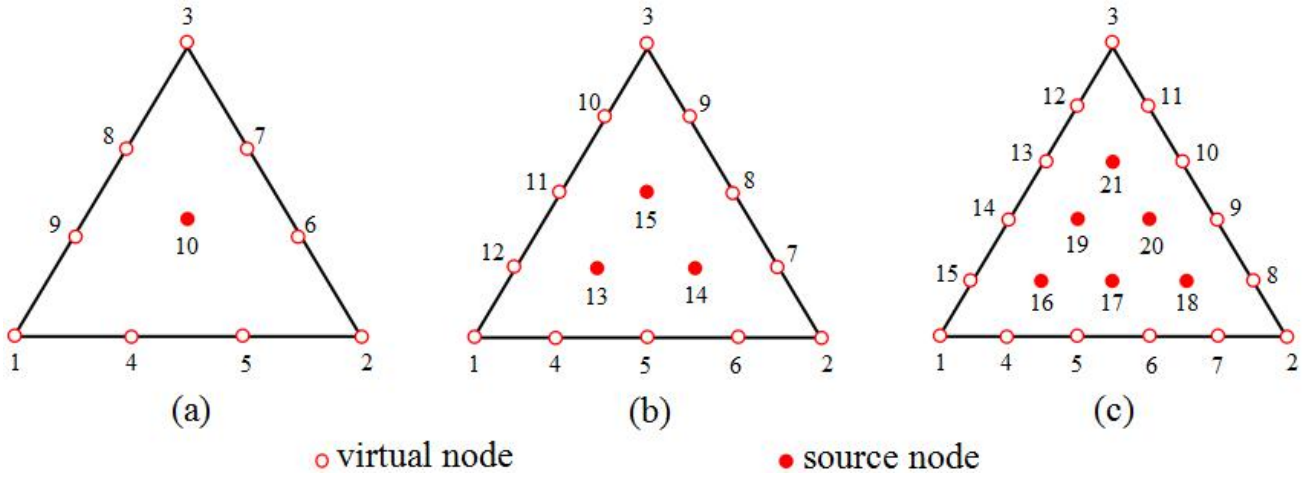

Fig. 3. dual interpolation triangle elements for 3-D problems: (a) TS1, (b) TS3, and (c) TS6.

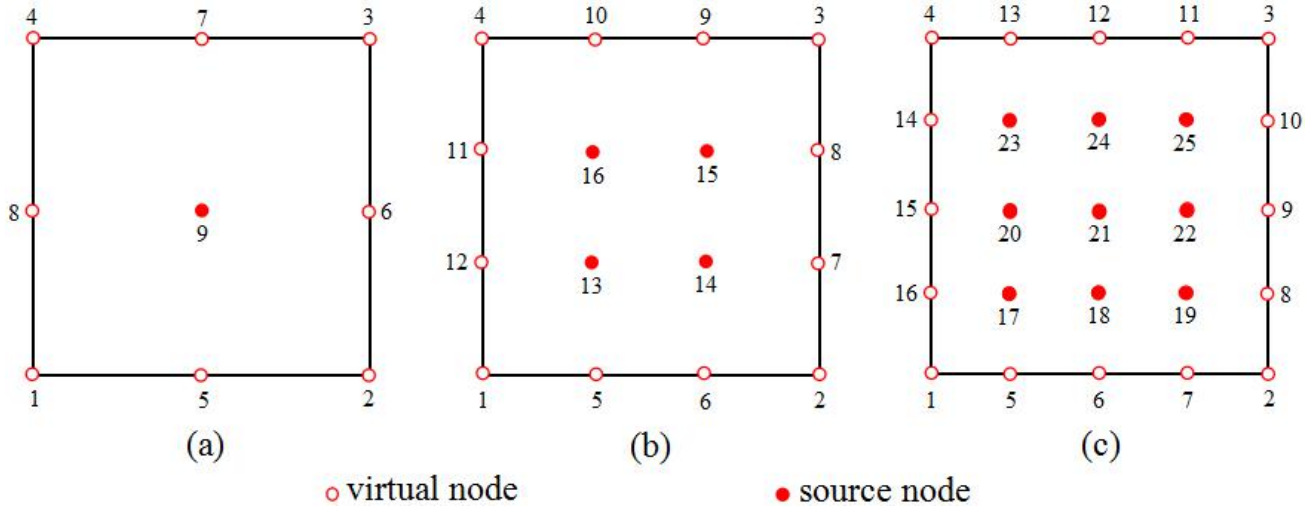

Fig. 4. dual interpolation quadrilateral elements for 3-D problems: (a) QS1, (b) QS4, and (c) QS9.

In the DiBFM implementation, we introduce a new type of elements, called the dual interpolation elements. The dual interpolation elements are able to unify the conventional continuous and discontinuous elements. The dual interpolation elements are divided into different element types according to the order of element. As shown in Fig.3 and Fig.4, corresponding dual interpolation triangle elements (TS1, TS3 and TS6) and quadrilateral elements (QS1, QS4 and QS9) are a constant, linear, and quadratic element, respectively. The dual interpolation elements with the notation TS1, TS3, TS6 and QS1, QS4, QS9 denote the number of source nodes in a triangle or quadrilateral element. The shape functions for the constant dual interpolation elements TS1 in Fig.3(a) and QS1 in Fig.4(a) are provided in Eq. (4) and Eq. (5), respectively. Similarly, the shape functions for other dual interpolation triangle elements (TS3, TS6) and quadrilateral elements (QS4 and QS9) can be formulated in the same way as the standard elements of FEM or BEM on the basis of the scraping line method.

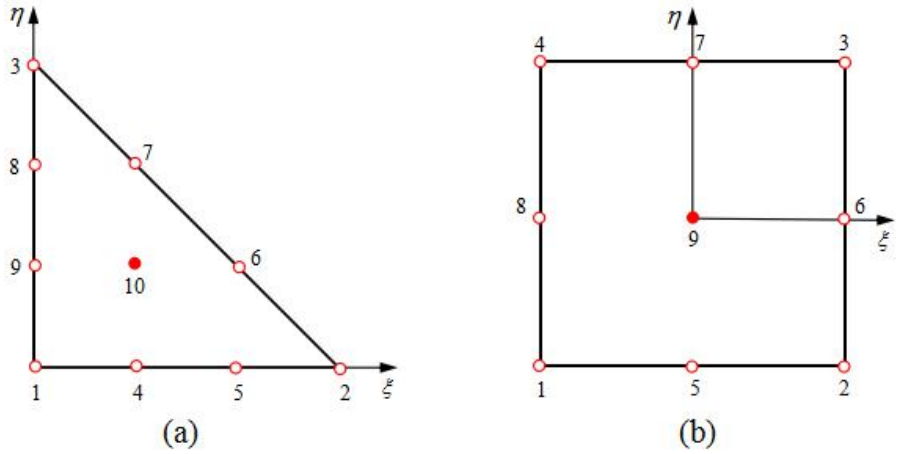

Fig. 5. Local parametric coordinates in the dual interpolation element: (a) TS1 and (b) QS1.

The shape functions for the dual interpolation element TS1

$$\begin{cases} N_1 = 0.5(3\xi-1)(3\xi-2)\xi, & N_6 = 4.5\eta(1-\xi-\eta)(3\eta-1), \\ N_2 = 0.5(3\eta-1)(3\eta-2)\eta, & N_7 = 4.5\eta(1-\xi-\eta)(2-3\xi-3\eta), \\ N_3 = 0.5(2-3\xi-3\eta)(1-3\xi-3\eta)(1-\xi-\eta), & N_8 = 4.5\xi(1-\xi-\eta)(2-3\xi-3\eta), \\ N_4 = 4.5\xi\eta(3\xi-1), & N_9 = 4.5\xi(1-\xi-\eta)(3\xi-1), \\ N_5 = 4.5\xi\eta(3\eta-1), & N_{10} = 27\xi\eta(1-\xi-\eta) \end{cases} \tag{4}$$

where ξ, η represent the natural coordinates defined on a triangle element, i.e. $\xi, \eta \in [0,1]$.

The shape functions for the dual interpolation element QS1

$$\begin{cases} N_1 = 0.25\xi\eta(\xi-1)(\eta-1), & N_5 = 0.5\eta(1-\xi^2)(\eta-1), \\ N_2 = 0.25\xi\eta(\xi+1)(\eta-1), & N_6 = 0.5\xi(\xi+1)(1-\eta^2), \\ N_3 = 0.25\xi\eta(\xi+1)(\eta+1), & N_7 = 0.5\eta(1-\xi^2)(\eta+1), \\ N_4 = 0.25\xi\eta(\xi-1)(\eta+1), & N_8 = 0.5\xi(\xi-1)(1-\eta^2), \\ & N_9 = (1-\xi^2)(1-\eta^2) \end{cases} \tag{5}$$

where ξ, η represent the natural coordinates defined on a quadrilateral element, i.e. $\xi, \eta \in [-1,1]$.

As is illustrated in Fig.3 and Fig.4, the red solid nodes inside the dual interpolation elements are marked as source nodes. The red hollow nodes on the boundary of the dual interpolation elements denote virtual nodes. Considering both source nodes and virtual nodes, the dual interpolation element is the same as a standard continuous element. Without taking into virtual nodes consideration, the dual interpolation element is equivalent to a standard discontinuous element. The order of interpolation function of the dual interpolation elements is increased at least by two orders compared with the conventional elements using the source nodes alone. As has been demonstrated numerically in Ref. [33], the dual interpolation elements exhibit higher accuracy and more superior convergence behavior than the conventional discontinuous elements. In addition, numerical results have demonstrated that the DiBFM is less sensitive to the quality of mesh generation. Even with some very irregular elements in the process of mesh generation, the DiBFM still has the ability to exhibit high accuracy and superior convergence behavior (see the second numerical example in Section 5 for details).

3.2 The first-layer interpolation

The boundary physical variables are interpolated by the first-layer interpolation in DiBFM, which is similar to the interpolation using the conventional continuous elements. The main difference

between them is that the shape functions of a dual interpolation element are drived by both source nodes and virtual nodes. For 3-D potential problems, the unknown quantities, i.e. the potential u and the normal flux q, at any point (ξ,η) in interpolating are evaluated by

$$u(\xi,\eta)=\sum_{\alpha=1}^{n\alpha}N_{\alpha}^{s}(\xi,\eta)u(Q_{\alpha}^{s})+\sum_{\beta=1}^{n\beta}N_{\beta}^{v}(\xi,\eta)u(Q_{\beta}^{v})\ , \tag{6}$$

$$q(\xi,\eta)=\sum_{\alpha=1}^{n\alpha}N_{\alpha}^{s}(\xi,\eta)q(Q_{\alpha}^{s})+\sum_{\beta=1}^{n\beta}N_{\beta}^{v}(\xi,\eta)q(Q_{\beta}^{v})\ , \tag{7}$$

where the superscripts s and v represent the source and virtual nodes, respectively. The subscripts α, β represent the α^{th} source and β^{th} virtual node in a dual interpolation element, respectively. $n\alpha$ and $n\beta$ denote the number of source nodes and virtual nodes in a dual interpolation element, respectively. $N_{\alpha}^{s}(\xi,\eta)$ and $N_{\beta}^{v}(\xi,\eta)$ are the shape functions for source nodes and virtual nodes, respectively. Note that the virtual nodal parameters $u(Q_{\beta}^{v})$ and $q(Q_{\beta}^{v})$ are not independent variables, which are interpolated by the second-layer interpolation in DiBFM.

3.3 The second-layer interpolation

Corresponding constraint equations using the MLS approximation are required to be formulated to condense the degrees of freedom for all virtual nodes in the second-layer interpolation. Besides, both continuous and discontinuous fields can be well approximated by determining the range of influence of an evaluating virtual node in MLS.

3.3.1. The moving least square approximation

Since all nodes of elements covered on the boundary $\partial\Omega$ of a 3-D domain Ω, the MLS approximation is calculated on the bounding surfaces directly. The MLS approximation is used to formulate relevant constraint equations between source nodes and virtual nodes. It should be noted that it is not necessary to evaluate the shape functions at each Gaussian point during the boundary integration.

Given a virtual node $Q_{\beta}^{v}=(\xi_{\beta}^{v},\eta_{\beta}^{v})$, the MLS interpolants u and q are defined as

$$u(Q_{\beta}^{v})=\sum_{j=1}^{M}\Phi_{j}^{s}(\xi_{\beta}^{v},\eta_{\beta}^{v})\hat{u}(Q_{j}^{s})\ , \tag{8}$$

$$q(Q_\beta^v) = \sum_{j=1}^{M} \Phi_j^s(\xi_\beta^v, \eta_\beta^v)\hat{q}(Q_j^s)\,, \tag{9}$$

where points Q_j^s are the source nodes on the boundary $\partial\Omega$, M is the number of source nodes in the vicinity of Q_β^v for which the weight functions $w(Q_\beta^v, Q_j^s) \neq 0$. It should be noted here that $\hat{u}(Q_j^s)$ and $\hat{q}(Q_j^s)$ used in Eqs. (8) and (9) are the fictitious nodal values, which are not equal to the nodal values $u(Q_j^s)$ and $q(Q_j^s)$ in general. $\Phi_j^s(\xi_\beta^v, \eta_\beta^v)$ ~~is the shape function of MLS approximation relating to the source node Q_j^s, which can be expressed as~~

~~$$\Phi_j^s(\xi_\beta^v, \eta_\beta^v) = \mathbf{p}^{\mathrm{T}}(\xi_\beta^v, \eta_\beta^v)[\mathbf{A}^{-1}(\xi_\beta^v, \eta_\beta^v)\mathbf{B}(\xi_\beta^v, \eta_\beta^v)]_{kj} \qquad (10)$$~~

For the shape functions of MLS approximation relating to all source nodes, which can be expressed as

$$\begin{aligned}\boldsymbol{\Phi} &= \left\{\Phi_1^s, \Phi_2^s, \cdots, \Phi_j^s, \cdots, \Phi_M^s\right\} \\ &= \mathbf{p}^{\mathrm{T}}(\xi,\eta)\mathbf{A}^{-1}(\xi,\eta)\mathbf{B}(\xi,\eta)\end{aligned} \tag{10}$$

with matrices $\mathbf{p}^{\mathrm{T}}(\xi,\eta)$, $\mathbf{A}(\xi,\eta)$ and $\mathbf{B}(\xi,\eta)$ defined by

$$\mathbf{p}^{\mathrm{T}} = [1,\ \xi,\ \eta,\ \xi^2,\ \xi\eta,\ \eta^2], \qquad m = 6$$

$$\mathbf{A}(\xi,\eta) = \sum_{j=1}^{M} w_j \mathbf{p}(\xi_j,\eta_j)\mathbf{p}^T(\xi_j,\eta_j)$$

$$\mathbf{B}(\xi,\eta) = \left[w_1\mathbf{p}(\xi_1,\eta_1),\ w_2\mathbf{p}(\xi_2,\eta_2),\ \ldots,\ w_M\mathbf{p}(\xi_M,\eta_M)\right]$$

where w_j is the weight function corresponding to a node (ξ_j,η_j). The $\Phi_j^s(\xi_\beta^v, \eta_\beta^v)$ is usually called the shape function of the MLS approximation corresponding to the source node Q_j^s.

The source nodes determined in the range of influence of the weight functions relating to an evaluating virtual node in MLS are obtained by searching several layer elements in the vicinity of the virtual node, rather than searching all source nodes on the boundary $\partial\Omega$ of domain, as is shown in Fig.6. More details of the MLS approximation are available in [37].

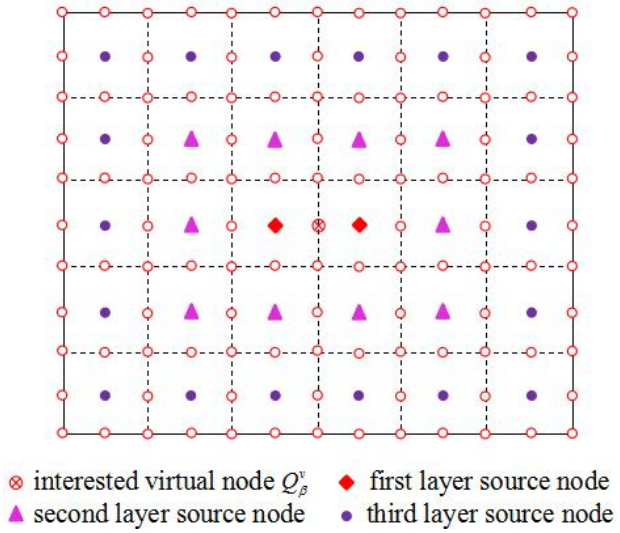

Fig. 6. The range of influence of an interested virtual node Q_β^v.

3.3.2. Approximation of continuous and discontinuous fields

By determining the range of influence of the weight functions corresponding to an evaluating virtual node in MLS, both continuous and discontinuous fields can be naturally and accurately approximated. To illustrate the particular feature of DiBFM, it will be explained by a schematic description for the continuous or discontinuous function approximation, as illustrated in Fig.7.

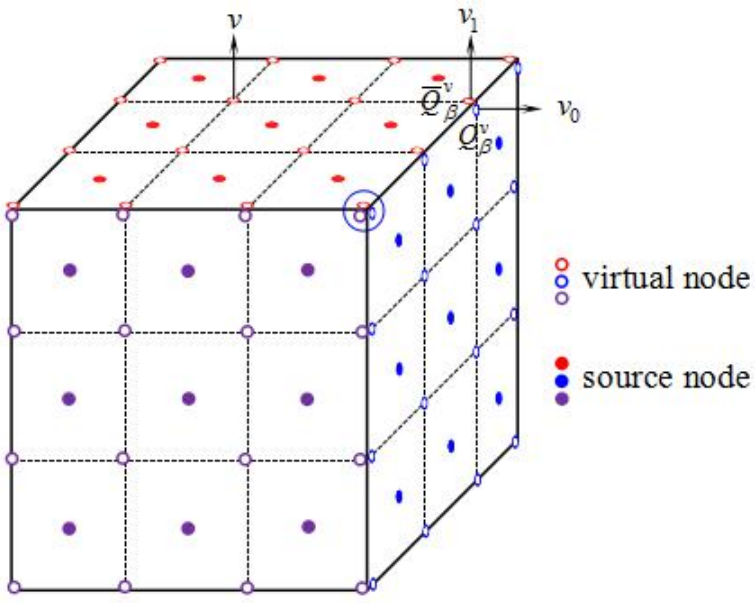

Fig. 7. Approximation of the continuous or discontinuous fields

For approximation of the continuous fields, only one virtual node v is distributed at the points of elements. When determining the range of influence of the weight functions in MLS, all source nodes in the vicinity of an evaluating virtual node are considered as valid nodes involved in computation.

For approximation of the discontinuous fields, multiple virtual nodes are distributed at the discontinuous boundary, such as geometric corners, non-smooth geometric boundary edges or element nodes at which the field is discontinuous. As depicted in Fig.7, two same co-ordinates virtual nodes v_0 and v_1 are placed on the non-smooth geometric boundary edge. These two virtual nodes lie on different boundary faces, one for each of the two adjacent faces, which making all boundary elements mutually independent and naturally for approximation of the discontinuous fields. When determining the range of influence of the weight functions in MLS for approximation of the discontinuous field at the virtual node Q_β^v, the virtual node $\overline{Q}_\beta^v$ is considered as a opaque node, namely, the source nodes of elements lying on other boundary faces beyond the opaque virtual node are not included. The range of influence of the virtual node v_0 covers the nine blue source nodes only, while the nine red source nodes are merely covered in the range of influence of the virtual node v_1.

In summary, the DiBFM presented in this section has several interesting properties.

(i) The dual interpolation elements exhibit higher accuracy and more superior convergence behavior than the conventional discontinuous elements.

(ii) Despite the introduction of virtual nodes in the dual interpolation elements, only source nodes of each element are taken as the collocation points. With the second-layer interpolation, the DiBFM does not result in the scale of final linear system increasing.

(iii) The dual interpolation elements have the ability to unify the conventional continuous and discontinuous elements, which can be able to well approximate both continuous and discontinuous fields.

(iV) Even with some irregular elements in numerical simulation, accurate numerical results and high convergence rates can be achieved by the DiBFM.

(V) In the DiBFM implementation, the geometric variables are calculated directly from the bounding surfaces rather than from elements, which makes a truly seamless interaction between CAD and CAE successfully achieved without any geometric simplification. The DiBFM could be an essential step for solving real world geometries in a fully automated manner based on this competitive advantage.

4. DiBFM for three-dimensional potential problem

4.1 Boundary-integral formulation

Consider an arbitrary 3-D domain Ω, as illustrated in Fig. 8, on which the potential problem governed by Laplace's equation with boundary conditions is given by (see e.g. [1] for details)

$$\begin{aligned} &\nabla^2 u = 0 \qquad \forall \boldsymbol{x} \in \Omega, \\ &u = \bar{u} \qquad \forall \boldsymbol{x} \in \Gamma_u, \\ &q = \frac{\partial u}{\partial n} = \bar{q} \quad \forall \boldsymbol{x} \in \Gamma_q, \end{aligned} \tag{11}$$

where Γ_u is the essential boundary, Γ_q is the flux boundary, $\bar{u}$ and $\bar{q}$ are prescribed Dirichlet and Neumann boundary conditions on Γ_u and Γ_q, respectively, and n is the outward normal vector.

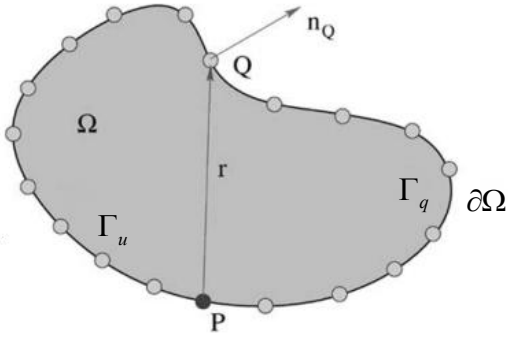

Fig. 8. An arbitrary domain on which the potential equation is to be solved.

The boundary integral equation (BIE) for three-dimensional potential problem is written as

$$c(P)u(P) = \int_\Gamma G(P,Q)q(Q)d\Gamma - \int_\Gamma \frac{\partial G(P,Q)}{\partial n(Q)} u(Q)d\Gamma, \qquad P,Q \in \Gamma \tag{12}$$

where the coefficient $c(P)$ is expressed as

$$c(P) = \begin{cases} 1 & P \text{ in the interior region of } \Omega \\ 0.5 & P \text{ on the boundary } \partial\Omega \\ 0 & P \text{ in the exterior region of } \Omega \end{cases} \tag{13}$$

and P is the source point, Q is the field point, the Green's function $G(P,Q)$ is the fundamental solutions. For three-dimensional potential problems, the Green's function is given by

$$G(P,Q) = \frac{1}{4\pi} \cdot \frac{1}{r(P,Q)}, \tag{14}$$

with $r(P,Q)$ being the distance between P and Q in three dimensions.

4.2 Discretization of the BIE for potential problems

In the DiBFM, the boundary of domain is discretized into the dual interpolation elements. For three-dimensional potential problems, the discretization form of the BIE of Eq. (12) can be written as

$$\sum_{j=1}^{ne}\left[\sum_{\alpha=1}^{n\alpha}h_{ij}^{ss}(P_i)u_j(Q_\alpha^s)+\sum_{\beta=1}^{n\beta}h_{ij}^{sv}(P_i)u_j(Q_\beta^v)\right]=\sum_{j=1}^{ne}\left[\sum_{\alpha=1}^{n\alpha}g_{ij}^{ss}(P_i)q_j(Q_\alpha^s)+\sum_{\beta=1}^{n\beta}g_{ij}^{sv}(P_i)q_j(Q_\beta^v)\right], \tag{15}$$

in which the entries of the coefficients in Eq. (15) are given by

$$h_{ij}^{ss}(P)=\int_{\Gamma_j}\frac{\partial G(P,Q)}{\partial n(Q)}N_{j(\alpha)}^s(Q)d\Gamma(Q)+\frac{1}{2}\delta_{ij}^{\alpha}, \tag{16}$$

$$h_{ij}^{sv}(P)=\int_{\Gamma_j}\frac{\partial G(P,Q)}{\partial n(Q)}N_{j(\beta)}^v(Q)d\Gamma(Q), \tag{17}$$

$$g_{ij}^{ss}(P)=\int_{\Gamma_j}G(P,Q)N_{j(\alpha)}^s(Q)d\Gamma(Q), \tag{18}$$

$$g_{ij}^{sv}(P)=\int_{\Gamma_j}G(P,Q)N_{j(\beta)}^v(Q)d\Gamma(Q), \tag{19}$$

and

$$\delta_{ij}^{\alpha}=\begin{cases}1, & \text{if source node } P \text{ is located at the } \alpha^{\text{th}} \text{ source node in the } j^{\text{th}} \text{ element}\\ 0, & \end{cases}, \tag{20}$$

where ne, NS and NP denote the total number of elements, source nodes and field nodes on the boundary of domain, respectively. $N_{j(\alpha)}^s(Q)$, $N_{j(\beta)}^v(Q)$ denote the shape functions for α^{th} source node and β^{th} virtual node of the j^{th} dual interpolation element, respectively.

Eq. (15) can be rewritten in a matrix form as

$$\mathbf{Hu}=\mathbf{Gq}, \tag{21}$$

where $\mathbf{H}$ and $\mathbf{G}$ are $NS\times NP$ coefficient matrices, $\mathbf{u}$ and $\mathbf{q}$ are $NP\times 1$ potential and its normal derivative vector, respectively.

To facilitate the derivation procedure, the coefficient matrices $\mathbf{H}$ and $\mathbf{G}$ in Eq. (21) are decomposed as

$$\begin{bmatrix} \mathbf{H}_{dd}^{ss} & \mathbf{H}_{dr}^{ss} & \mathbf{H}_{dn}^{ss} & \mathbf{H}_{dd}^{sv} & \mathbf{H}_{dr}^{sv} & \mathbf{H}_{dn}^{sv} \\ \mathbf{H}_{rd}^{ss} & \mathbf{H}_{rr}^{ss} & \mathbf{H}_{rn}^{ss} & \mathbf{H}_{rd}^{sv} & \mathbf{H}_{rr}^{sv} & \mathbf{H}_{rn}^{sv} \\ \mathbf{H}_{nd}^{ss} & \mathbf{H}_{nr}^{ss} & \mathbf{H}_{nn}^{ss} & \mathbf{H}_{nd}^{sv} & \mathbf{H}_{nr}^{sv} & \mathbf{H}_{nn}^{sv} \end{bmatrix} \begin{Bmatrix} \overline{\mathbf{u}}_d^s \\ \tilde{\mathbf{u}}_r^s \\ \mathbf{u}_n^s \\ \overline{\mathbf{u}}_d^v \\ \tilde{\mathbf{u}}_r^v \\ \mathbf{u}_n^v \end{Bmatrix} = \begin{bmatrix} \mathbf{G}_{dd}^{ss} & \mathbf{G}_{dr}^{ss} & \mathbf{G}_{dn}^{ss} & \mathbf{G}_{dd}^{sv} & \mathbf{G}_{dr}^{sv} & \mathbf{G}_{dn}^{sv} \\ \mathbf{G}_{rd}^{ss} & \mathbf{G}_{rr}^{ss} & \mathbf{G}_{rn}^{ss} & \mathbf{G}_{rd}^{sv} & \mathbf{G}_{rr}^{sv} & \mathbf{G}_{rn}^{sv} \\ \mathbf{G}_{nd}^{ss} & \mathbf{G}_{nr}^{ss} & \mathbf{G}_{nn}^{ss} & \mathbf{G}_{nd}^{sv} & \mathbf{G}_{nr}^{sv} & \mathbf{G}_{nn}^{sv} \end{bmatrix} \begin{Bmatrix} \mathbf{q}_d^s \\ \tilde{\mathbf{q}}_r^s \\ \overline{\mathbf{q}}_n^s \\ \mathbf{q}_d^v \\ \tilde{\mathbf{q}}_r^v \\ \overline{\mathbf{q}}_n^v \end{Bmatrix} \tag{22}$$

where the subscripts *d*, *n* and *r* of the submatrices of $\mathbf{H}$ and $\mathbf{G}$ denote the Dirichlet, Neumann and Robin boundary conditions, respectively. $\overline{\mathbf{u}}$ and $\overline{\mathbf{q}}$ are the described potential and normal flux vectors, respectively.

4.3 Condensation of degrees of freedom for virtual nodes

Since the boundary integral equations in DiBFM are collocated at the source nodes only, the number of unknown nodal values is more than the number of equations (see Eq. (22)). The constraint equations of the degrees of freedom for all virtual nodes should be constructed, which are used to add the number of equations and make them be equal. If the virtual nodes are imposed the boundary conditions, the boundary variables at these nodes can be obtained directly. The unknown potential in $\mathbf{u}^v$ and normal flux $\mathbf{q}^v$ of virtual nodes can be approximated by the second-layer interpolation. The matrix forms of $\mathbf{u}^v$ and $\mathbf{q}^v$ are expressed as

$$\begin{Bmatrix} \tilde{\mathbf{u}}_r^v \\ \mathbf{u}_n^v \end{Bmatrix} = \begin{bmatrix} \mathbf{\Psi}_{rr}^{vs} & \mathbf{\Psi}_{rn}^{vs} \\ \mathbf{\Psi}_{nr}^{vs} & \mathbf{\Psi}_{nn}^{vs} \end{bmatrix} \begin{Bmatrix} \tilde{\mathbf{u}}_r^s \\ \mathbf{u}_n^s \end{Bmatrix} = \mathbf{\Psi}^{vs} \begin{Bmatrix} \tilde{\mathbf{u}}_r^s \\ \mathbf{u}_n^s \end{Bmatrix} \tag{23}$$

$$\mathbf{q}_d^v = \mathbf{\Theta}_{dd}^{vs} \mathbf{q}_d^s \tag{24}$$

where $\mathbf{\Psi}_{rr}^{vs}$, $\mathbf{\Psi}_{rn}^{vs}$, $\mathbf{\Psi}_{nr}^{vs}$, $\mathbf{\Psi}_{nn}^{vs}$ and $\mathbf{\Theta}_{dd}^{vs}$ are shape function matrices of the second-layer interpolation, which are constructed by the MLS approximation, as is mentioned in Section 3.3.

The degrees of freedom for $\tilde{\mathbf{q}}_r^v$ can be condensed using the Robin boundary condition

$$\tilde{\mathbf{q}}_r^v = \boldsymbol{\beta}_r^v - \boldsymbol{\alpha}_r^v \tilde{\mathbf{u}}_r^v, \tag{25}$$

and substituting Eq. (25) into Eq. (22) , gives

$$\begin{bmatrix} \mathbf{H}_{dd}^{ss} & \mathbf{H}_{dr}^{ss} & \mathbf{H}_{dn}^{ss} & \mathbf{H}_{dd}^{sv} & \mathbf{H}_{dr}^{sv}+\mathbf{G}_{dr}^{sv}\boldsymbol{\alpha}_r^v & \mathbf{H}_{dn}^{sv} \\ \mathbf{H}_{rd}^{ss} & \mathbf{H}_{rr}^{ss} & \mathbf{H}_{rn}^{ss} & \mathbf{H}_{rd}^{sv} & \mathbf{H}_{rr}^{sv}+\mathbf{G}_{rr}^{sv}\boldsymbol{\alpha}_r^v & \mathbf{H}_{rn}^{sv} \\ \mathbf{H}_{nd}^{ss} & \mathbf{H}_{nr}^{ss} & \mathbf{H}_{nn}^{ss} & \mathbf{H}_{nd}^{sv} & \mathbf{H}_{nr}^{sv}+\mathbf{G}_{nr}^{sv}\boldsymbol{\alpha}_r^v & \mathbf{H}_{nn}^{sv} \end{bmatrix} \begin{Bmatrix} \overline{\mathbf{u}}_d^s \\ \tilde{\mathbf{u}}_r^s \\ \mathbf{u}_n^s \\ \overline{\mathbf{u}}_d^v \\ \tilde{\mathbf{u}}_r^v \\ \mathbf{u}_n^v \end{Bmatrix} = \begin{bmatrix} \mathbf{G}_{dd}^{ss} & \mathbf{G}_{dr}^{ss} & \mathbf{G}_{dn}^{ss} & \mathbf{G}_{dd}^{sv} & \mathbf{G}_{dn}^{sv} \\ \mathbf{G}_{rd}^{ss} & \mathbf{G}_{rr}^{ss} & \mathbf{G}_{rn}^{ss} & \mathbf{G}_{rd}^{sv} & \mathbf{G}_{rn}^{sv} \\ \mathbf{G}_{nd}^{ss} & \mathbf{G}_{nr}^{ss} & \mathbf{G}_{nn}^{ss} & \mathbf{G}_{nd}^{sv} & \mathbf{G}_{nn}^{sv} \end{bmatrix} \begin{Bmatrix} \mathbf{q}_d^s \\ \tilde{\mathbf{q}}_r^s \\ \overline{\mathbf{q}}_n^s \\ \mathbf{q}_d^v \\ \overline{\mathbf{q}}_n^v \end{Bmatrix} + \begin{bmatrix} \mathbf{G}_{dr}^{sv} \\ \mathbf{G}_{rr}^{sv} \\ \mathbf{G}_{nr}^{sv} \end{bmatrix} \boldsymbol{\beta}_r^v, \tag{26}$$

Substituting the approximations for $\tilde{\mathbf{u}}_r^v, \mathbf{u}_n^v$ and $\mathbf{q}_d^v$ into Eq. (26) using Eqs. (23) and (24).

$$\begin{bmatrix} \bar{\mathbf{H}}_{dd}^{ss} & \bar{\mathbf{H}}_{dr}^{ss} & \bar{\mathbf{H}}_{dn}^{ss} & \mathbf{H}_{dd}^{sv} \\ \bar{\mathbf{H}}_{rd}^{ss} & \bar{\mathbf{H}}_{rr}^{ss} & \bar{\mathbf{H}}_{rn}^{ss} & \mathbf{H}_{rd}^{sv} \\ \bar{\mathbf{H}}_{nd}^{ss} & \bar{\mathbf{H}}_{nr}^{ss} & \bar{\mathbf{H}}_{nn}^{ss} & \mathbf{H}_{nd}^{sv} \end{bmatrix} \begin{Bmatrix} \overline{\mathbf{u}}_d^s \\ \tilde{\mathbf{u}}_r^s \\ \mathbf{u}_n^s \\ \overline{\mathbf{u}}_d^v \end{Bmatrix} = \begin{bmatrix} \bar{\mathbf{G}}_{dd}^{ss} & \bar{\mathbf{G}}_{dr}^{ss} & \bar{\mathbf{G}}_{dn}^{ss} & \mathbf{G}_{dn}^{sv} \\ \bar{\mathbf{G}}_{rd}^{ss} & \bar{\mathbf{G}}_{rr}^{ss} & \bar{\mathbf{G}}_{rn}^{ss} & \mathbf{G}_{rn}^{sv} \\ \bar{\mathbf{G}}_{nd}^{ss} & \bar{\mathbf{G}}_{nr}^{ss} & \bar{\mathbf{G}}_{nn}^{ss} & \mathbf{G}_{nn}^{sv} \end{bmatrix} \begin{Bmatrix} \mathbf{q}_d^s \\ \tilde{\mathbf{q}}_r^s \\ \overline{\mathbf{q}}_n^s \\ \overline{\mathbf{q}}_n^v \end{Bmatrix} + \begin{bmatrix} \mathbf{G}_{dr}^{sv} \\ \mathbf{G}_{rr}^{sv} \\ \mathbf{G}_{nr}^{sv} \end{bmatrix} \boldsymbol{\beta}_r^v, \tag{27}$$

in which

$$\begin{bmatrix} \bar{\mathbf{H}}_{dd}^{ss} & \bar{\mathbf{H}}_{dr}^{ss} & \bar{\mathbf{H}}_{dn}^{ss} \\ \bar{\mathbf{H}}_{rd}^{ss} & \bar{\mathbf{H}}_{rr}^{ss} & \bar{\mathbf{H}}_{rn}^{ss} \\ \bar{\mathbf{H}}_{nd}^{ss} & \bar{\mathbf{H}}_{nr}^{ss} & \bar{\mathbf{H}}_{nn}^{ss} \end{bmatrix} = \begin{bmatrix} \mathbf{H}_{dd}^{ss} & \mathbf{H}_{dr}^{ss} & \mathbf{H}_{dn}^{ss} \\ \mathbf{H}_{rd}^{ss} & \mathbf{H}_{rr}^{ss} & \mathbf{H}_{rn}^{ss} \\ \mathbf{H}_{nd}^{ss} & \mathbf{H}_{nr}^{ss} & \mathbf{H}_{nn}^{ss} \end{bmatrix} + \begin{bmatrix} \mathbf{H}_{dr}^{sv}+\mathbf{G}_{dr}^{sv}\boldsymbol{\alpha}_r^v & \mathbf{H}_{dn}^{sv} \\ \mathbf{H}_{rr}^{sv}+\mathbf{G}_{rr}^{sv}\boldsymbol{\alpha}_r^v & \mathbf{H}_{rn}^{sv} \\ \mathbf{H}_{nr}^{sv}+\mathbf{G}_{nr}^{sv}\boldsymbol{\alpha}_r^v & \mathbf{H}_{nn}^{sv} \end{bmatrix} \begin{bmatrix} \boldsymbol{\Psi}_{rr}^{vs} & \boldsymbol{\Psi}_{rn}^{vs} \\ \boldsymbol{\Psi}_{nr}^{vs} & \boldsymbol{\Psi}_{nn}^{vs} \end{bmatrix}, \tag{28}$$

$$\begin{bmatrix} \bar{\mathbf{G}}_{dd}^{ss} & \bar{\mathbf{G}}_{dn}^{ss} & \bar{\mathbf{G}}_{dn}^{sv} \\ \bar{\mathbf{G}}_{rd}^{ss} & \bar{\mathbf{G}}_{rn}^{ss} & \bar{\mathbf{G}}_{rn}^{sv} \\ \bar{\mathbf{G}}_{nd}^{ss} & \bar{\mathbf{G}}_{nn}^{ss} & \bar{\mathbf{G}}_{nn}^{sv} \end{bmatrix} = \begin{bmatrix} \mathbf{G}_{dd}^{ss} & \mathbf{G}_{dn}^{ss} & \mathbf{G}_{dn}^{sv} \\ \mathbf{G}_{rd}^{ss} & \mathbf{G}_{rn}^{ss} & \mathbf{G}_{rn}^{sv} \\ \mathbf{G}_{nd}^{ss} & \mathbf{G}_{nn}^{ss} & \mathbf{G}_{nn}^{sv} \end{bmatrix} + \begin{Bmatrix} \mathbf{G}_{dd}^{sv} \\ \mathbf{G}_{rd}^{sv} \\ \mathbf{G}_{nd}^{sv} \end{Bmatrix} \boldsymbol{\Theta}_{dd}^{vs}, \tag{29}$$

Substituting the described boundary conditions $\overline{\mathbf{u}}_d^v$ and $\overline{\mathbf{q}}_n^v$ of virtual nodes into Eq. (27).

$$\begin{bmatrix} \bar{\mathbf{H}}_{dd}^{ss} & \bar{\mathbf{H}}_{dr}^{ss} & \bar{\mathbf{H}}_{dn}^{ss} \\ \bar{\mathbf{H}}_{rd}^{ss} & \bar{\mathbf{H}}_{rr}^{ss} & \bar{\mathbf{H}}_{rn}^{ss} \\ \bar{\mathbf{H}}_{nd}^{ss} & \bar{\mathbf{H}}_{nr}^{ss} & \bar{\mathbf{H}}_{nn}^{ss} \end{bmatrix} \begin{Bmatrix} \overline{\mathbf{u}}_d^s \\ \tilde{\mathbf{u}}_r^s \\ \mathbf{u}_n^s \end{Bmatrix} = \begin{bmatrix} \bar{\mathbf{G}}_{dd}^{ss} & \bar{\mathbf{G}}_{dr}^{ss} & \bar{\mathbf{G}}_{dn}^{ss} \\ \bar{\mathbf{G}}_{rd}^{ss} & \bar{\mathbf{G}}_{rr}^{ss} & \bar{\mathbf{G}}_{rn}^{ss} \\ \bar{\mathbf{G}}_{nd}^{ss} & \bar{\mathbf{G}}_{nr}^{ss} & \bar{\mathbf{G}}_{nn}^{ss} \end{bmatrix} \begin{Bmatrix} \mathbf{q}_d^s \\ \tilde{\mathbf{q}}_r^s \\ \overline{\mathbf{q}}_n^s \end{Bmatrix} + \begin{bmatrix} -\mathbf{H}_{dd}^{sv} & \mathbf{G}_{dn}^{sv} \\ -\mathbf{H}_{rd}^{sv} & \mathbf{G}_{rn}^{sv} \\ -\mathbf{H}_{nd}^{sv} & \mathbf{G}_{nn}^{sv} \end{bmatrix} \begin{Bmatrix} \overline{\mathbf{u}}_d^v \\ \overline{\mathbf{q}}_n^v \end{Bmatrix} + \begin{bmatrix} \mathbf{G}_{dr}^{sv} \\ \mathbf{G}_{rr}^{sv} \\ \mathbf{G}_{nr}^{sv} \end{bmatrix} \boldsymbol{\beta}_r^v, \tag{30}$$

Similarly, applying the Robin boundary condition $\tilde{\mathbf{q}}_r^s = \boldsymbol{\beta}_r^s - \boldsymbol{\alpha}_r^s \tilde{\mathbf{u}}_r^s$ into Eq. (30), we can obtain

$$\begin{bmatrix} \bar{\mathbf{H}}_{dd}^{ss} & \bar{\mathbf{H}}_{dr}^{ss}+\bar{\mathbf{G}}_{dr}^{ss}\boldsymbol{\alpha}_r^s & \bar{\mathbf{H}}_{dn}^{ss} \\ \bar{\mathbf{H}}_{rd}^{ss} & \bar{\mathbf{H}}_{rr}^{ss}+\bar{\mathbf{G}}_{rr}^{ss}\boldsymbol{\alpha}_r^s & \bar{\mathbf{H}}_{rn}^{ss} \\ \bar{\mathbf{H}}_{nd}^{ss} & \bar{\mathbf{H}}_{nr}^{ss}+\bar{\mathbf{G}}_{nr}^{ss}\boldsymbol{\alpha}_r^s & \bar{\mathbf{H}}_{nn}^{ss} \end{bmatrix} \begin{Bmatrix} \overline{\mathbf{u}}_d^s \\ \tilde{\mathbf{u}}_r^s \\ \mathbf{u}_n^s \end{Bmatrix} = \begin{bmatrix} \bar{\mathbf{G}}_{dd}^{ss} & \bar{\mathbf{G}}_{dr}^{ss} & \bar{\mathbf{G}}_{dn}^{ss} \\ \bar{\mathbf{G}}_{rd}^{ss} & \bar{\mathbf{G}}_{rr}^{ss} & \bar{\mathbf{G}}_{rn}^{ss} \\ \bar{\mathbf{G}}_{nd}^{ss} & \bar{\mathbf{G}}_{nr}^{ss} & \bar{\mathbf{G}}_{nn}^{ss} \end{bmatrix} \begin{Bmatrix} \mathbf{q}_d^s \\ \boldsymbol{\beta}_r^s \\ \overline{\mathbf{q}}_n^s \end{Bmatrix} + \begin{bmatrix} -\mathbf{H}_{dd}^{sv} & \mathbf{G}_{dn}^{sv} \\ -\mathbf{H}_{rd}^{sv} & \mathbf{G}_{rn}^{sv} \\ -\mathbf{H}_{nd}^{sv} & \mathbf{G}_{nn}^{sv} \end{bmatrix} \begin{Bmatrix} \overline{\mathbf{u}}_d^v \\ \overline{\mathbf{q}}_n^v \end{Bmatrix} + \begin{bmatrix} \mathbf{G}_{dr}^{sv} \\ \mathbf{G}_{rr}^{sv} \\ \mathbf{G}_{nr}^{sv} \end{bmatrix} \boldsymbol{\beta}_r^v, \tag{31}$$

4.4 Solution for potential problems

The final linear system for potential problems derived from Eq. (31) can be expressed as

$$\mathbf{A}\mathbf{x} = \mathbf{b}, \tag{32}$$

in which

$$\mathbf{A}=\begin{bmatrix} -\bar{\mathbf{G}}_{dd}^{ss} & \bar{\mathbf{H}}_{dr}^{ss}+\bar{\mathbf{G}}_{dr}^{ss}\boldsymbol{\alpha}_r^s & \bar{\mathbf{H}}_{dn}^{ss} \\ -\bar{\mathbf{G}}_{rd}^{ss} & \bar{\mathbf{H}}_{rr}^{ss}+\bar{\mathbf{G}}_{rr}^{ss}\boldsymbol{\alpha}_r^s & \bar{\mathbf{H}}_{rn}^{ss} \\ -\bar{\mathbf{G}}_{nd}^{ss} & \bar{\mathbf{H}}_{nr}^{ss}+\bar{\mathbf{G}}_{nr}^{ss}\boldsymbol{\alpha}_r^s & \bar{\mathbf{H}}_{rr}^{ss} \end{bmatrix}\begin{Bmatrix} \mathbf{q}_d^s \\ \tilde{\mathbf{u}}_r^s \\ \mathbf{u}_n^s \end{Bmatrix},$$

$$\mathbf{x}^{\mathrm{T}}=\begin{Bmatrix} \mathbf{q}_d^s & \tilde{\mathbf{u}}_r^s & \mathbf{u}_n^s \end{Bmatrix},$$

$$\mathbf{b}=\begin{bmatrix} -\bar{\mathbf{H}}_{dd}^{ss} & \bar{\mathbf{G}}_{dr}^{ss} & \bar{\mathbf{G}}_{dn}^{ss} \\ -\bar{\mathbf{H}}_{rd}^{ss} & \bar{\mathbf{G}}_{rr}^{ss} & \bar{\mathbf{G}}_{rn}^{ss} \\ -\bar{\mathbf{H}}_{nd}^{ss} & \bar{\mathbf{G}}_{nr}^{ss} & \bar{\mathbf{G}}_{nn}^{ss} \end{bmatrix}\begin{Bmatrix} \bar{\mathbf{u}}_d^s \\ \boldsymbol{\beta}_r^s \\ \bar{\mathbf{q}}_n^s \end{Bmatrix}+\begin{bmatrix} -\mathbf{H}_{dd}^{sv} & \mathbf{G}_{dn}^{sv} \\ -\mathbf{H}_{rd}^{sv} & \mathbf{G}_{rn}^{sv} \\ -\mathbf{H}_{nd}^{sv} & \mathbf{G}_{nn}^{sv} \end{bmatrix}\begin{Bmatrix} \mathbf{u}_d^v \\ \mathbf{q}_n^v \end{Bmatrix}+\begin{bmatrix} \mathbf{G}_{dr}^{sv} \\ \mathbf{G}_{rr}^{sv} \\ \mathbf{G}_{nr}^{sv} \end{bmatrix}\boldsymbol{\beta}_r^v ,$$

where $\mathbf{A}$ is the $NS\times NS$ coefficient matrix, $\mathbf{x}$ is the unknown $NS\times 1$ potential and its normal derivative of all source nodes vector, $\mathbf{b}$ is a known right-hand-side vector.

Using the LU decomposition to solve Eq. (32), the unknown potential and its normal derivative of all source nodes can be computed on each dual interpolation element. By using the dual interpolation elements, high accuracy and superior convergence can be affirmitived in DiBFM. It is worth to note that the scale of final linear system in DiBFM is equivalent to that in the conventional discontinuous element implementation.

5. Numerical examples

In this section, three numerical examples are given to demonstrate the accuracy and efficiency of the DiBFM for solving 3-D potential problems. The first example is given to demonstrate the accuracy and convergence rate of the DiBFM. The calculational results of other two examples are used to verify the availability that the DiBFM can be applied to complex geometries. Three examples with different boundary conditions are presented. Unless otherwise mentioned, q_m denotes the modulus of the vector (q_x, q_y, q_z), i.e. $q_m=\sqrt{q_x^2+q_y^2+q_z^2}$. The convergence of the method is measured by the relative error measure.

$$e=\frac{1}{|v|_{\max}}\sqrt{\frac{1}{N}\sum_{i=1}^{N}[v_i^{(e)}-v_i^{(n)}]^2}\ , \tag{33}$$

H1-norm: $e=\dfrac{1}{N}\sum_{i=1}^{N}\left|v_i^{(e)}-v_i^{(n)}\right|$

L2-norm: $e=\sqrt{\dfrac{1}{N}\sum_{i=1}^{N}[v_i^{(e)}-v_i^{(n)}]^2}$

where $|v|_{\max}$ is the maximum value of potential u_i or normal flux q_i over N sample points, and the superscripts (*e*) and (*n*) denote the exact and numerical solutions, respectively.

5.1 Mixed problems on a cube

The first example is a mixed problem on a cube with cubic polynomial solution for u. Consider the solution of a Laplace's equation on a cube that is bounded by the surfaces $x = \pm 1$, $y = \pm 1$ and $z = \pm 1$. Eq. (34) is used as the exact solution. Corresponding to the exact solution, a mixed problem is solved for which the essential boundary condition is imposed on faces $z = \pm 1$, and the natural boundary condition on faces $x = \pm 1$ and $y = \pm 1$.

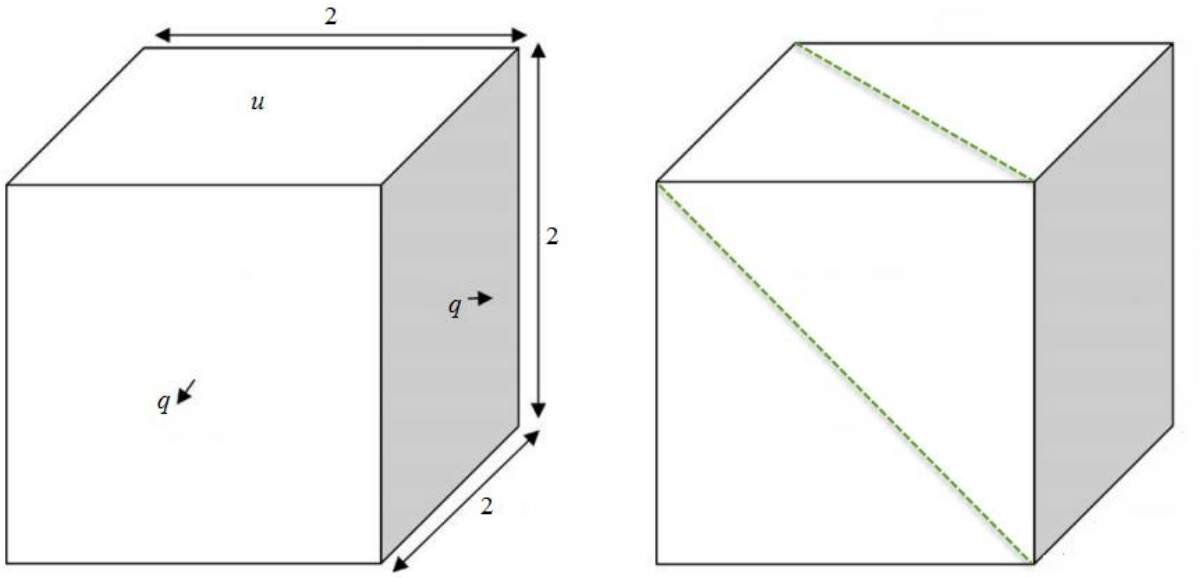

Fig. 9. A mixed problem on a cube: (a) geometry and boundary conditions of a cube, (b) distribution of the sample points on the diagonal of faces for u and q_m.

The potential boundary conditions are

$$u = x^3 + y^3 + z^3 - 3x^2y - 3y^2z - 3z^2x. \tag{34}$$

This example is presented to verify the accuracy and convergence performance of the DiBFM. To study the convergence of the DiBFM, a mixed problem on a cube has been tested through the dual interpolation element QS1 and TS1, respectively. This problem is solved by the DiBFM with 16, 100, 400 and 1600 quadrilateral elements per face, and 22, 102, 405 and 1610 triangular elements per face to study the convergence behavior. Nodes are uniformly distributed on the boundary of the domain. The numerical results have been obtained for various locations of the collocation points on the

boundary of the cube. A comparison of convergence of the DiBFM with the interpolation elements QS1 and TS1 (denoted by DiBFM QS1 and DiBFM TS1, respectively) is shown in Fig. 10 and Fig.11. The L_2 errors of nodal values presented in Table 1 for u (denoted by Err_u) and q_m (denoted by Err_q_m) are evaluated by Eq. (33) with different number of source nodes and different types of the constant dual interpolation elements. The results of the DiBFM with totally 600 QS1 elements and 610 TS1 elements are shown in Fig. 12 and Fig. 13. Comparison of the accuracy of the dual interpolation elements QS1 and TS1 for u (see Fig. 12) are evaluated over 200 sample points uniformly distributed from (1, -1, 1) to (1, 1, -1). The numerical results of q_m is shown in Fig. 13 employing a uniform distribution of same sample points along a straight line from (-1, -1, 1) to (1, 1, 1).

我们的评判误差公式

Table 1 Comparison of convergence of the DiBFM with the dual interpolation elements QS1 and TS1 for a mixed problem with cubic exact solution.

DiBFM QS1			DiBFM TS1		
NS	Err_u	Err_q_m	*NS*	Err_u	Err_q_m
96	7.59E-03	1.96E-02	132	6.98E-03	2.51E-02
600	3.23E-04	2.23E-03	612	3.83E-04	3.69E-03
2400	3.02E-05	4.22E-04	2430	6.46E-05	9.80E-04
9600	2.95E-06	8.37E-05	9660	5.67E-06	1.99E-04

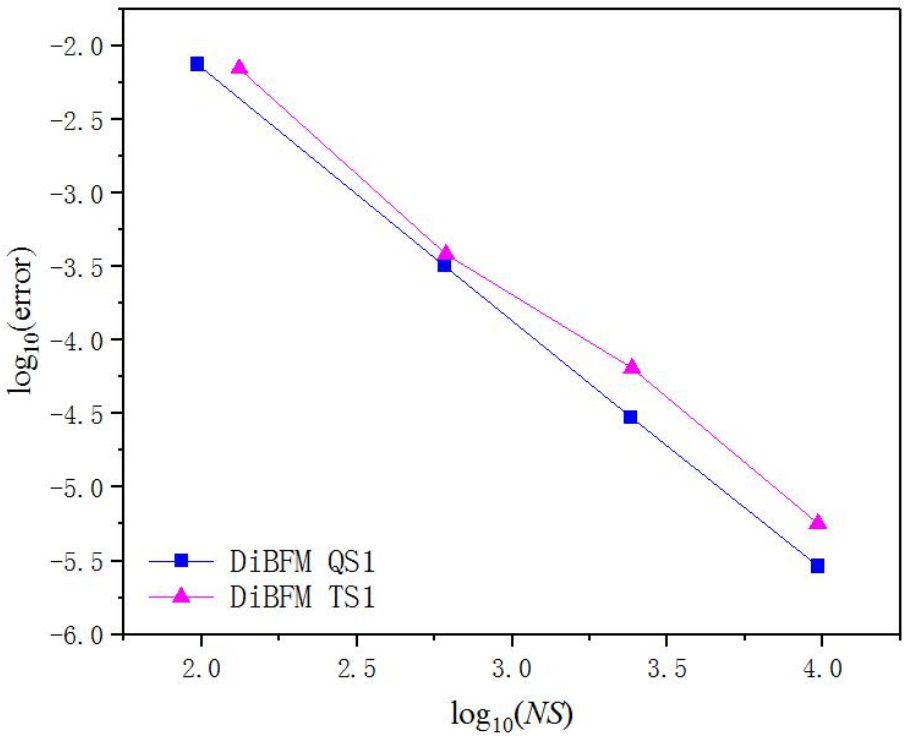

Fig. 10. Comparison of convergence of the DiBFM with the dual interpolation elements QS1 and TS1 for a mixed problem with cubic exact solution for u.

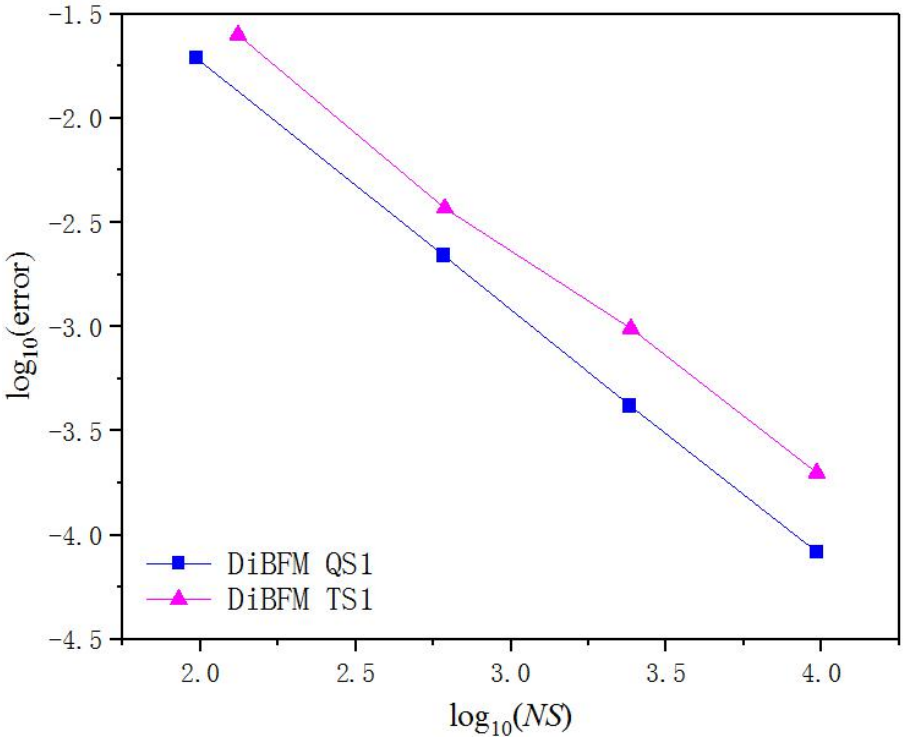

Fig. 11. Comparison of convergence of the DiBFM with the dual interpolation elements QS1 and TS1 for a mixed problem with cubic exact solution for q_m.

L2 范数

Table 2 Comparison of convergence of the DiBFM with the dual interpolation elements QS1 and TS1 for a mixed problem with cubic exact solution.

DiBFM QS1			DiBFM TS1		
NS	Err_u	Err_q_m	*NS*	Err_u	Err_q_m
96	4.55E-02	2.04E-01	132	4.18E-02	2.61E-01
600	1.93E-03	2.31E-02	612	2.29E-03	3.84E-02
2400	1.81E-04	4.38E-03	2430	3.87E-04	5.02E-03
9600	1.77E-05	5.70E-04 (8.70E-04)	9660	3.41E-05	7.06E-04 (2.06E-03)

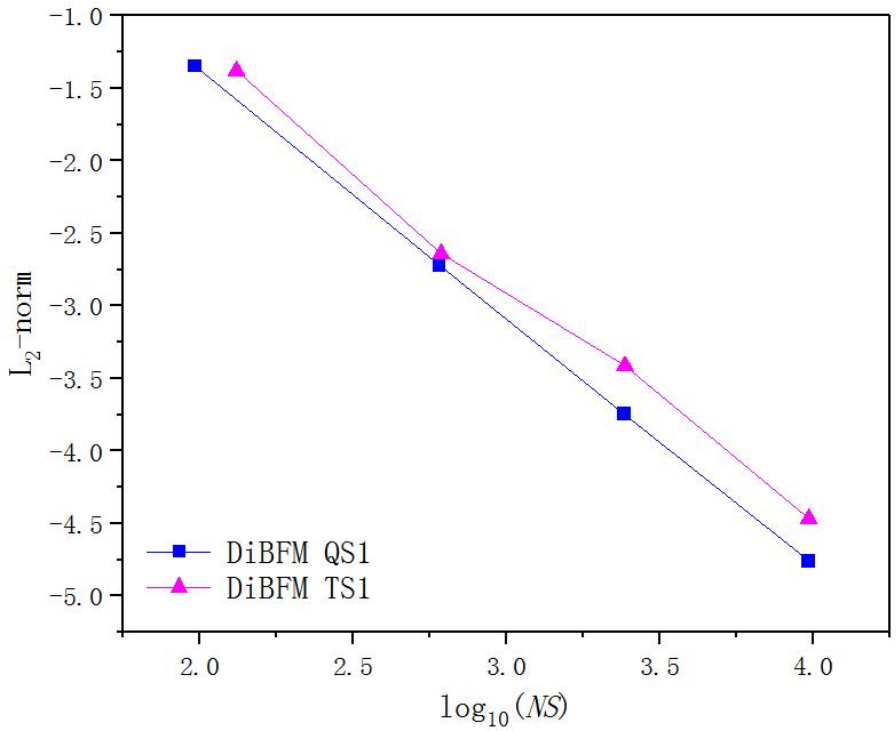

Fig. 10. Comparison of convergence of the DiBFM with the dual interpolation elements QS1 and TS1 for a mixed problem with cubic exact solution for u .

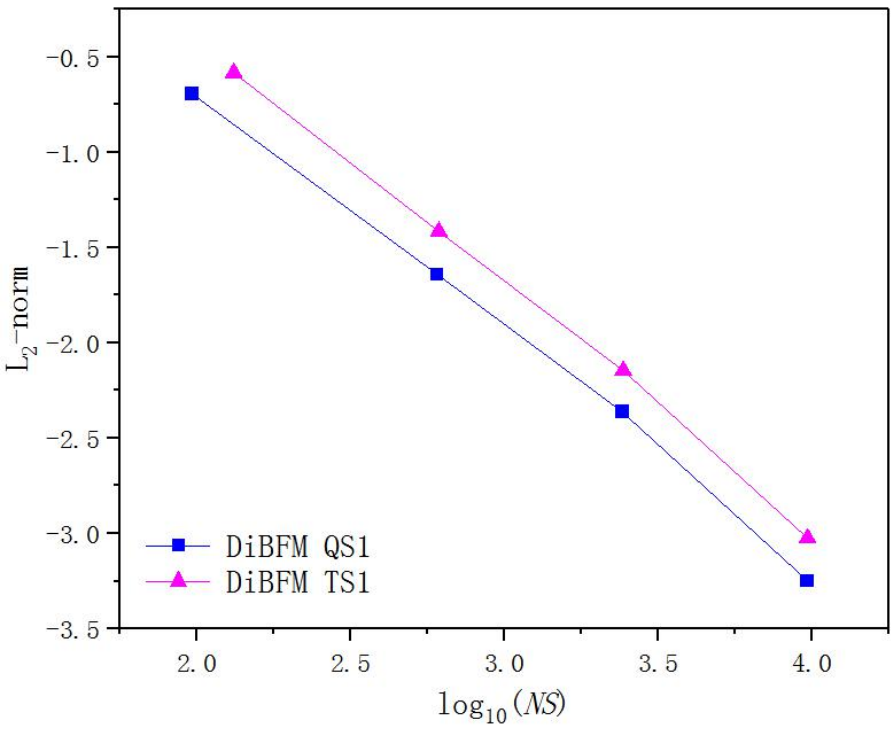

Fig. 11. Comparison of convergence of the DiBFM with the dual interpolation elements QS1 and TS1 for a mixed problem with cubic exact solution for q_m.

H1 范数

Table 3 Comparison of convergence of the DiBFM with the dual interpolation elements QS1 and TS1 for a mixed problem with cubic exact solution.

DiBFM QS1			DiBFM TS1		
NS	Err_u	Err_q_m	*NS*	Err_u	Err_q_m
96	2.43E-02	1.26E-01	132	2.52E-02	1.71E-01
600	8.92E-04	1.23E-02	612	1.63E-03	2.69E-02
2400	7.94E-05	2.39E-03	2430	2.43E-04	5.15E-03 (7.15E-03)
9600	7.45E-06	3.11E-04 (5.11E-04)	9660	2.35E-05	7.42E-04 (1.45E-03)

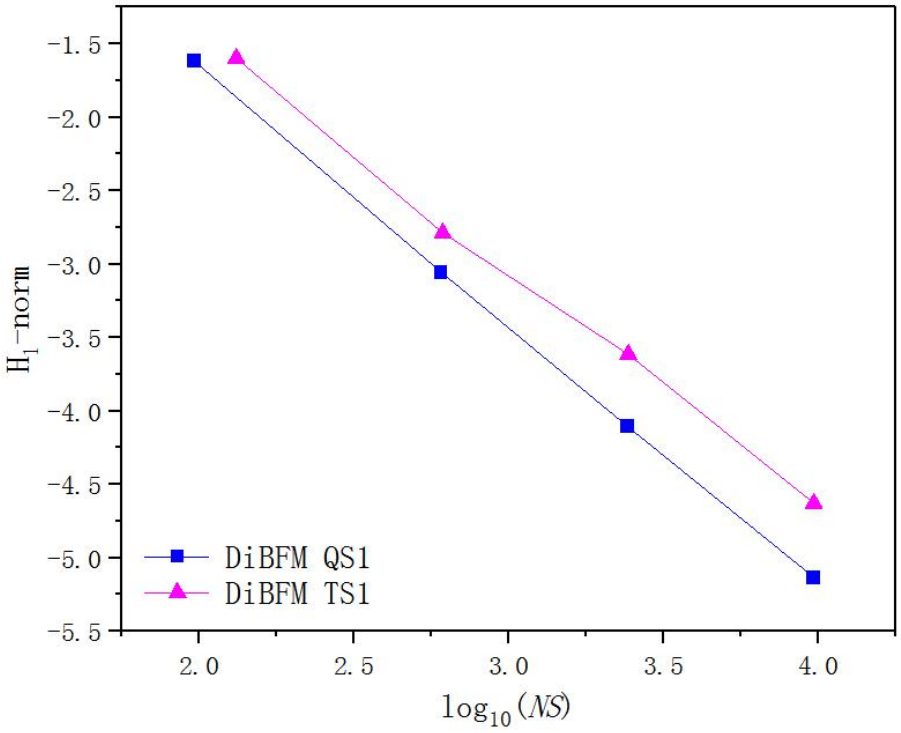

Fig. 10. Comparison of convergence of the DiBFM with the dual interpolation elements QS1 and TS1 for a mixed problem with cubic exact solution for u .

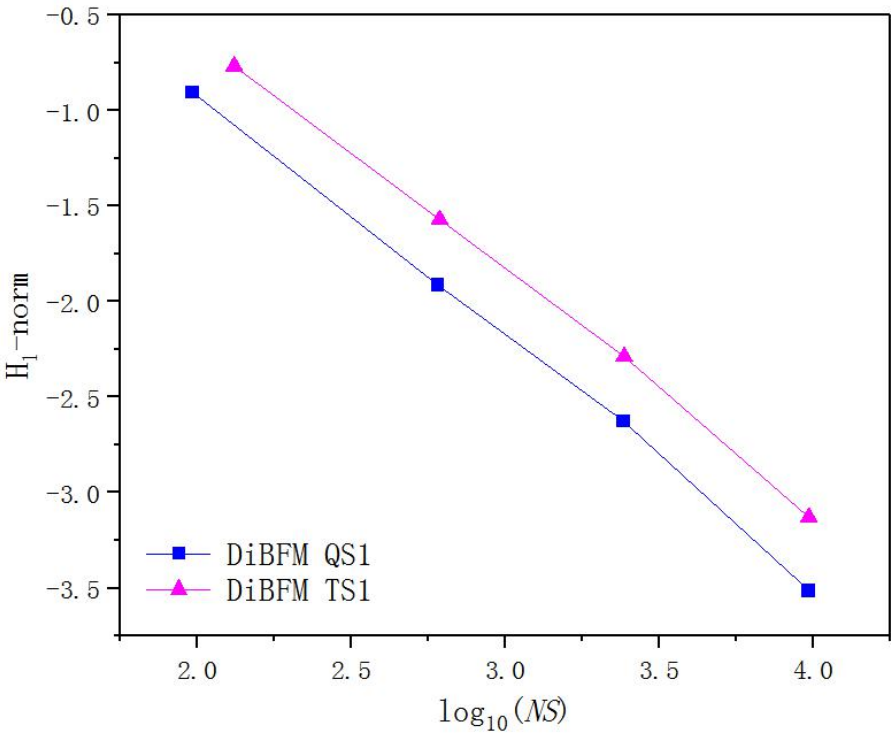

Fig. 11. Comparison of convergence of the DiBFM with the dual interpolation elements QS1 and TS1 for a mixed problem with cubic exact solution for q_m.

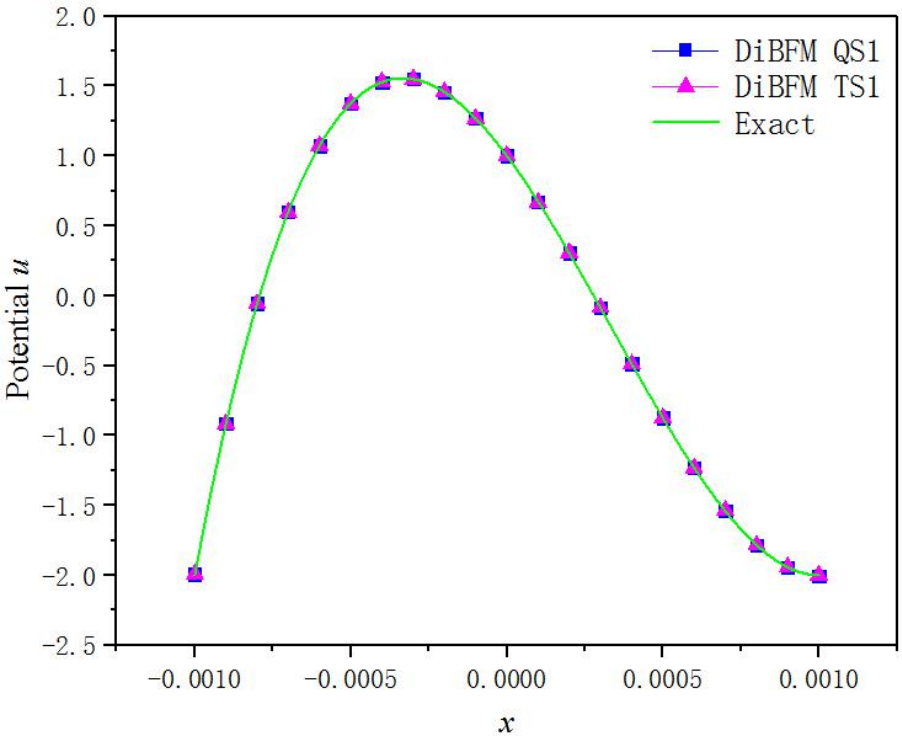

Fig. 12. Comparison of the accuracy of the DiBFM with the dual interpolation elements QS1 and TS1 for u on the diagonal of the face $x=1$.

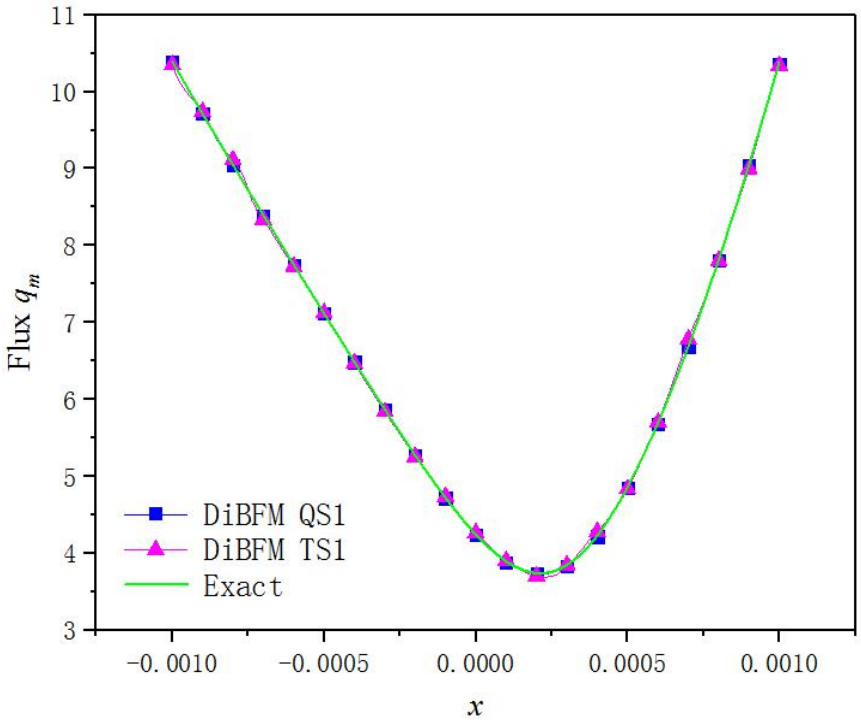

Fig. 13. Comparison of the accuracy of the DiBFM with the dual interpolation elements QS1 and TS1 for q_m on the diagonal of the face $z=1$.

As is illustrated in Fig. 10 and Fig.11, accuracy of the DiBFM for u and q_m is greatly improved

with the increasing number of all source nodes on the boundary of the cube. And above all, from the numerical results listed in Table 1, it can be seen that the convergence rate of these two types of the dual interpolation elements is similar when the number of source nodes used is almost the same. In the DiBFM, it is appealing that very high accuracy can be achieved. The numerical results of u and q_m in Fig. 12 and Fig.13 almost reproduce the analytical solution exactly, which further demonstrate the validity of the dual interpolation elements. It clearly shows that the DiBFM has excellent properties of high accuracy and superior convergence.

5.2 Dirichlet problems on a trimmed torus

The second example is a Dirichlet problem on a trimmed torus of major radius 3 and minor radius 1 centered at the point (2, 0, 0) with a cubic solution for u . The torus is trimmed by two spheres with a radius of 1.5 and two cylinders with the diameter of 1 in their bottom faces. As is depicted in Fig. 14, the coordinates of center of these two spheres are (-1, 0, 0) and (5, 0, 0), respectively. Two cylinder faces in a top view are centered at (2, 0, -2) and (2, 0, 2), respectively. The usual polar coordinates θ and φ are used for the torus. Dirichlet boundary conditions corresponding to the exact solution (Eq. (34)) are specified on all faces of the trimmed torus.

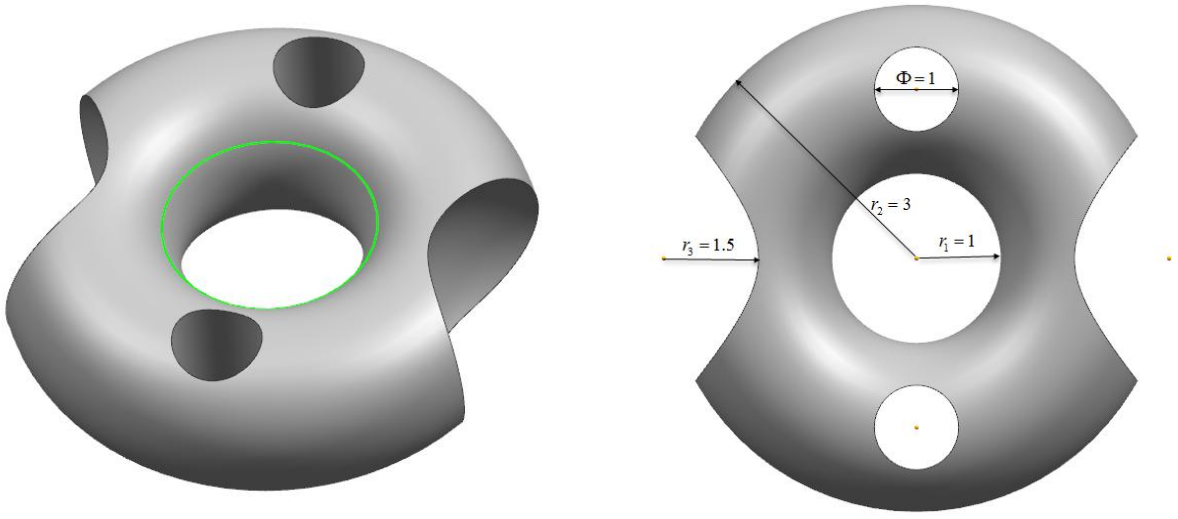

(a) Geometry and distribution of the sample points (b) Main dimensions of the torus

Fig. 14. Geometry of a trimmed torus.

This example is further demonstrated the accuracy and convergence performance of the DiBFM for complex geometries. It is also demonstrated that the DiBFM is less sensitive to the mesh density and mesh quality. As is well known that a key difficulty for mesh generation is to achieve the

connectivity requirements of the desirable mesh. Inevitably, there are some irregular elements on the trimmed spherical surface in the process of mesh generation (see Fig. 15), which is difficult to ensure the accuracy of numerical simulation.

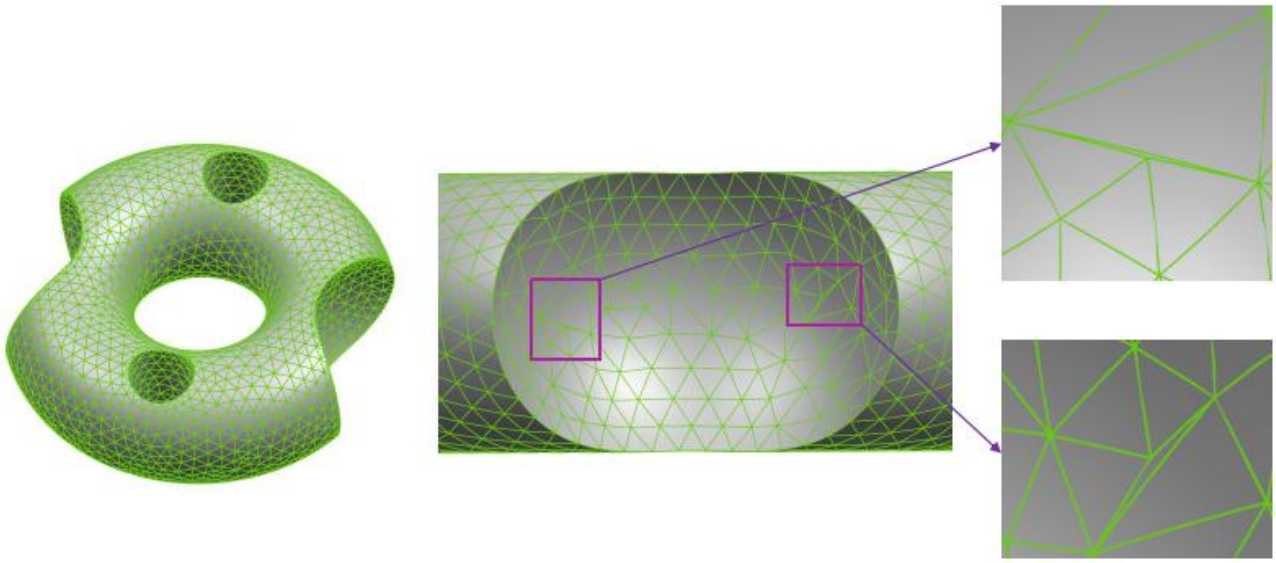

(a) (b) (c)

Fig. 15. Adaptive mesh generation of a trimmed torus: (a) the resulting mesh of the trimmed torus, (b) mesh generation of the trimmed spherical surface (c) the partial enlarged view of irregular elements.

To study the convergence behaviour of the DiBFM with irregular elements, this problem is solved using the TS1 elements with totally 1116, 2730, 5340 and 9820 source nodes, respectively. Corresponding convergence rate of the DiBFM with different number of source nodes for q_m is shown in Fig. 16. As is illustrated in Fig. 17 and Fig. 18, the numerical results of the DiBFM for u and q_m with totally 2730 TS1 elements are evaluated over 500 sample points uniformly distributed along a circle curve of radius 1.2 centered at the point (2, -0.6, 0) (see Fig. 14(a)). The relative errors for u and q_m on the surface are 0.0166% and 0.3718%, respectively. The potential and normal flux distribution in the whole domain are presented in Fig. 19.

我们的评判误差公式

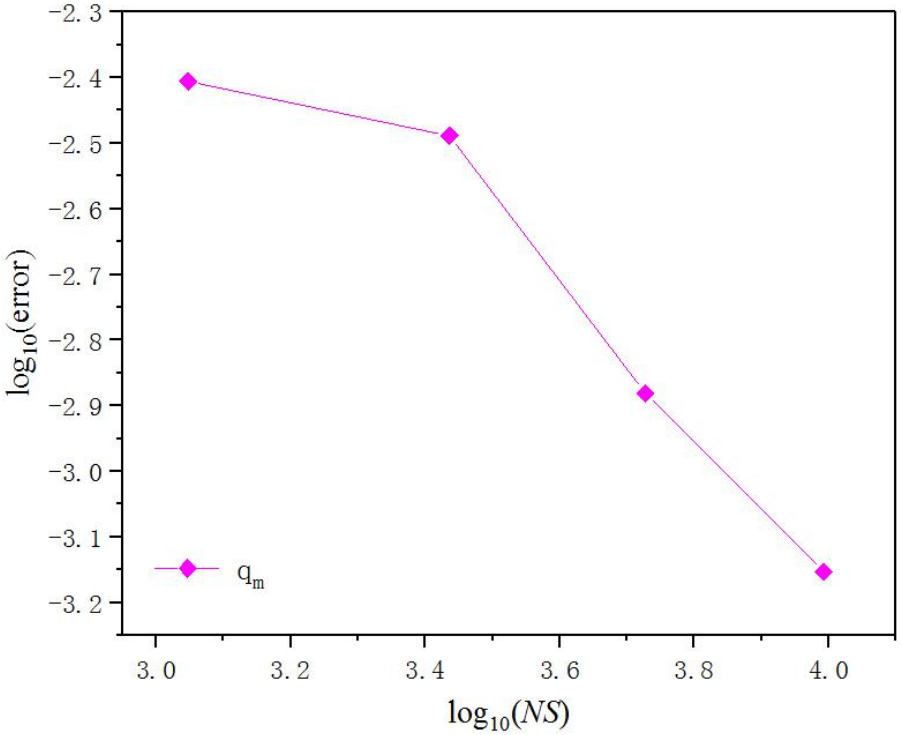

Fig. 16. Convergence of the DiBFM with TS1 elements for a Dirichlet problem with cubic exact solution for q_m.

L2 范数

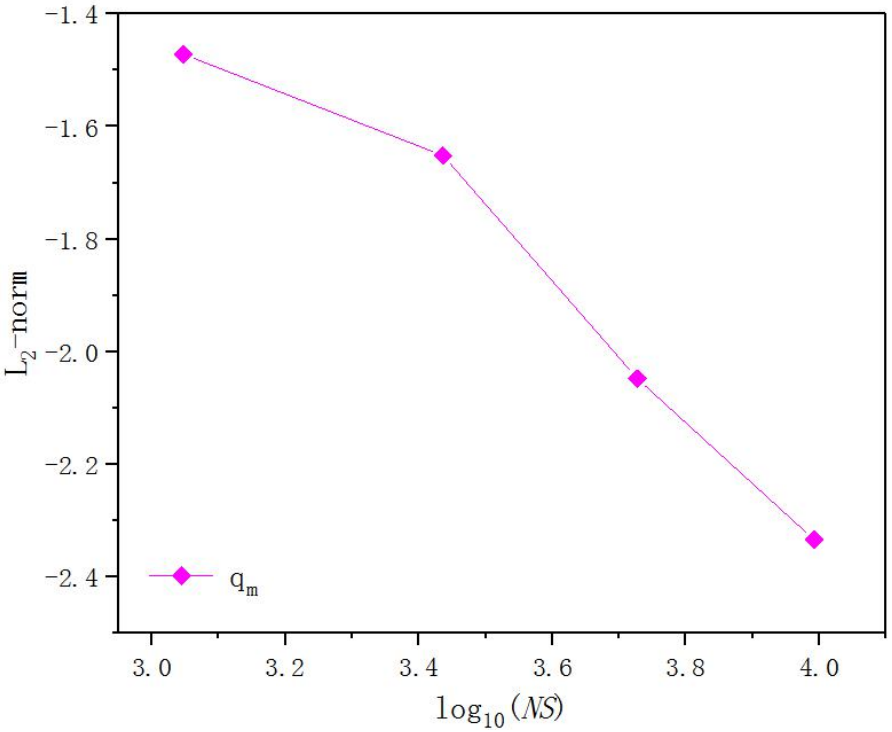

Fig. 16. Convergence of the DiBFM with TS1 elements for

a Dirichlet problem with cubic exact solution for q_m.

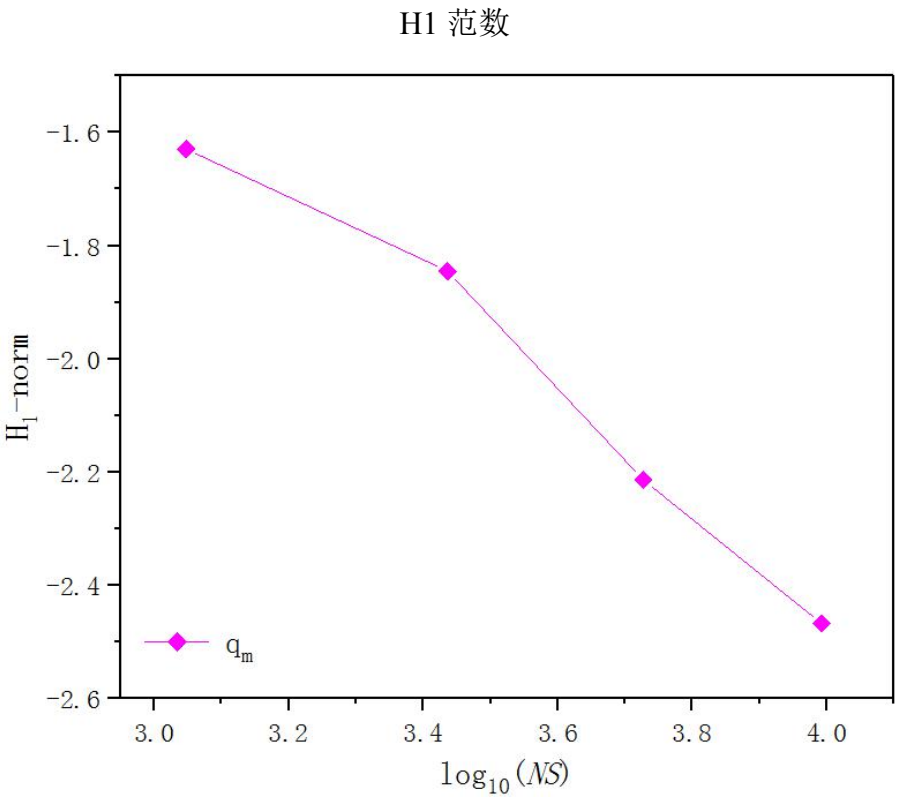

Fig. 16. Convergence of the DiBFM with TS1 elements for

a Dirichlet problem with cubic exact solution for q_m.

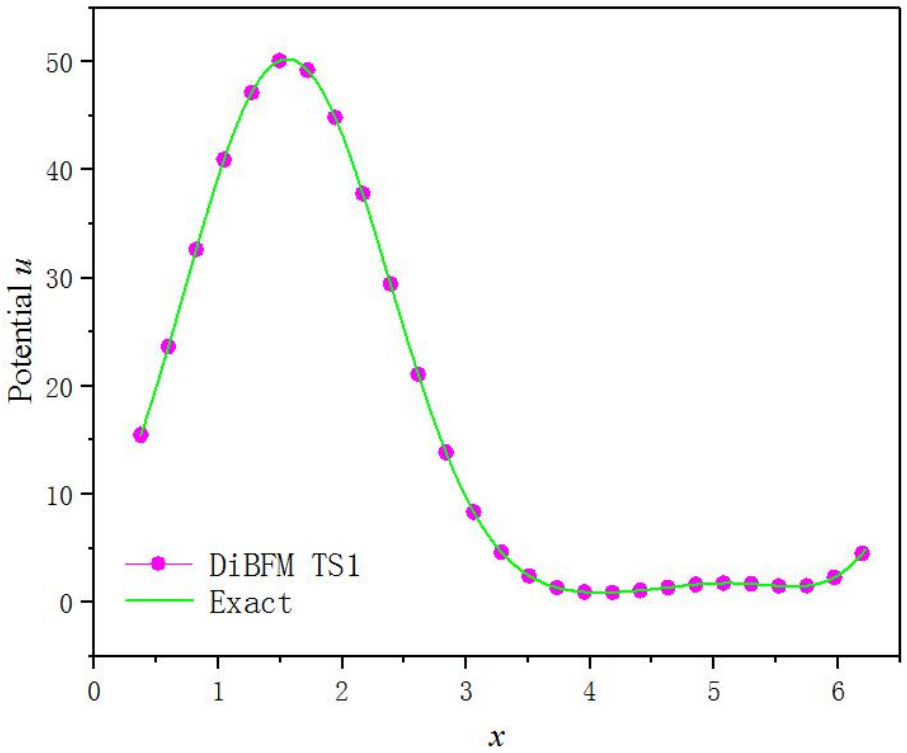

Fig. 17. Comparison of the accuracy of the DiBFM with TS1 elements for u along a circle curve.

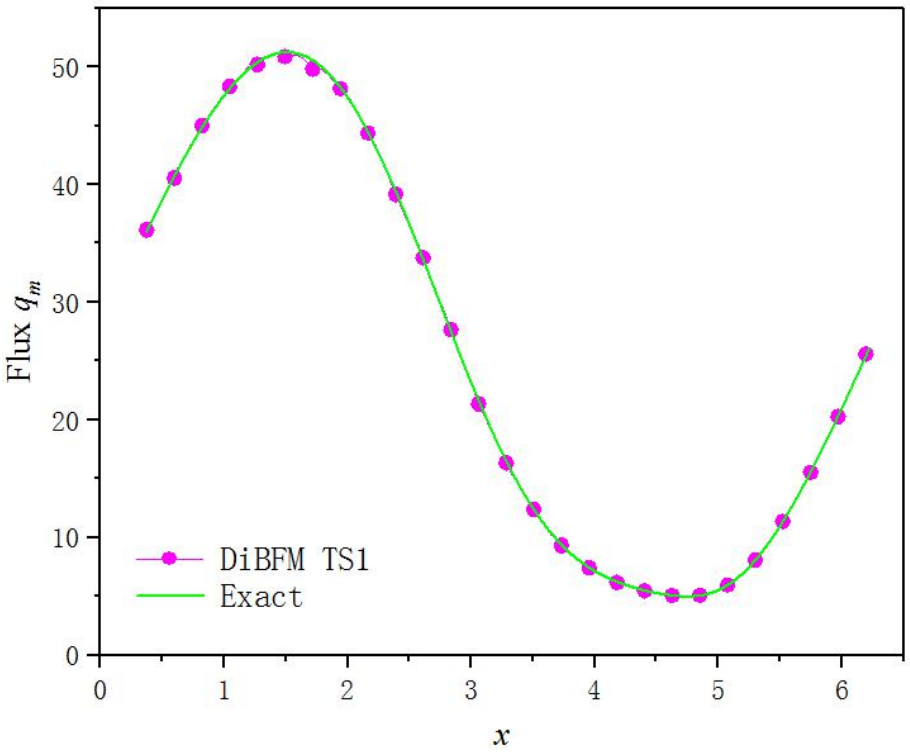

Fig. 18. Comparison of the accuracy of the DiBFM with TS1 elements for q_m along a circle curve.

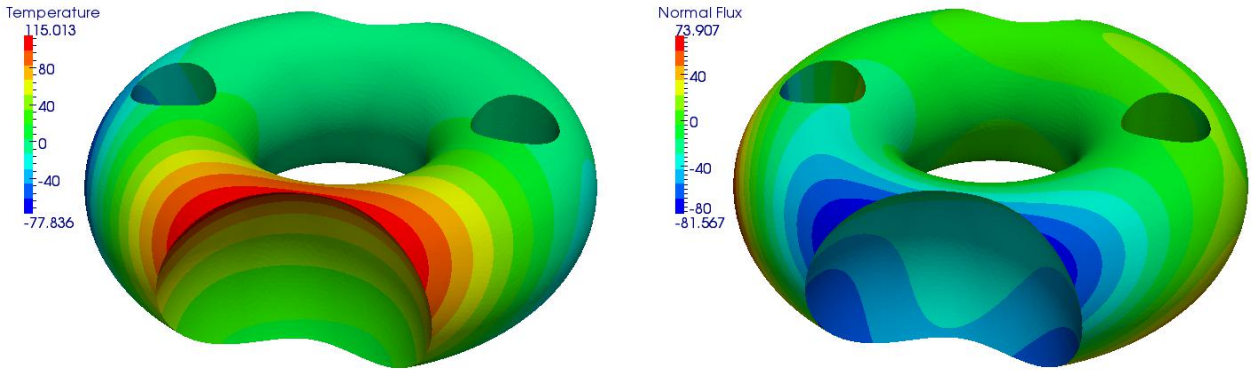

(a) The potential u distribution (b) The normal flux q distribution

Fig. 19. The contour plots of potential u and normal flux q in the whole domain.

It can be seen from Fig. 16 that even for the very irregular elements, high accuracy can be achieved by the DiBFM. The convergence rate of the DiBFM for u and q_m are still acceptable. With the increasing number of all source nodes on the boundary of the trimmed torus, accurate results and high convergence rates have been achieved. From Fig. 17 through Fig. 19, the numerical results of u and q_m obtained by the DiBFM with few source nodes are in good agreement with the exact solution, and are no more sensitive to irregular elements. This example clearly demonstrates the robustness of the DiBFM. The reason for high accuracy and superior convergence of the DiBFM is that both MLS and boundary integration are directly performed on boundary faces rather than from elements. No matter how coarse the discretization on the boundary of domain is, there are no geometric errors introduced in the DiBFM implementation.

5.3 Steady heat transfer analysis on a cup

To study the performance of the DiBFM in analysis of more complicated geometries, a steady heat transfer problem on a cup shown in Fig. 20(a) is investigated. The geometry and its main dimensions are illustrated in Fig. 20(b). As is depicted in Fig. 21(a), the cup model is subjected to Dirichlet, Neumann and Robin boundary conditions. Dirichlet boundary conditions are specified on the inner cylindrical surface and the planar surface. The bottom planar surface outside of the cup is regarded as adiabatic boundary, i.e. $q = 0$ W/m^2. Robin boundary conditions are specified on all other surfaces on the boundary of the cup. For the Dirichlet boundary, T=100°C, and for the Robin boundary, the heat transfer coefficient h is chosen to be 0.1 W/(m^2·°C), the ambient temperature is T_∞=20°C. The material parameter of heat conductivity is taken as k=1.2 W/(m·°C).

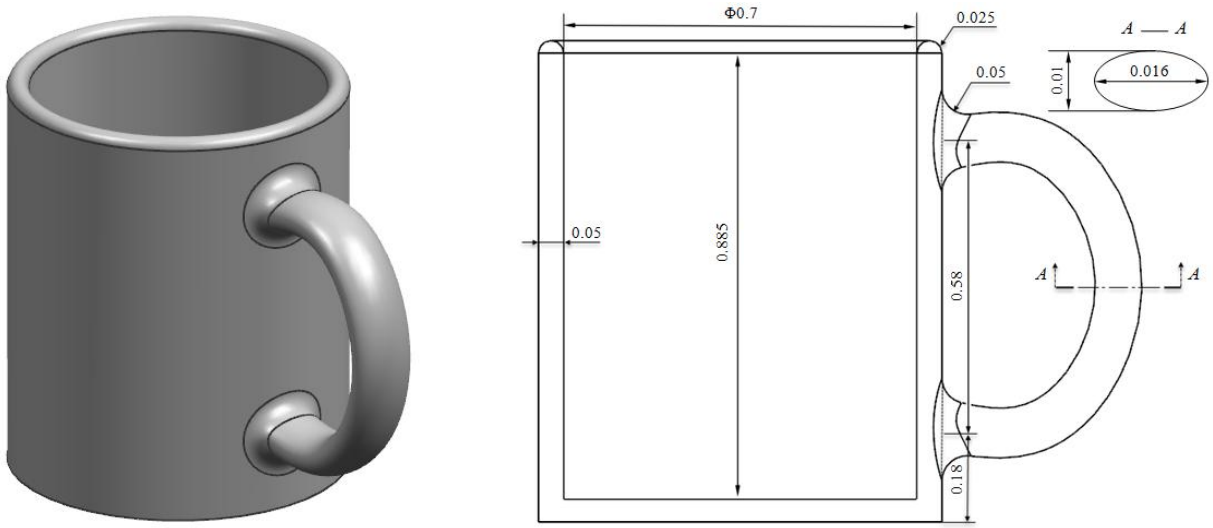

(a) Geometric model of a cup (b) Main dimensions of the cup

Fig. 20. Geometry of a cup.

This numerical example is presented to show the accuracy and convergence of the DiBFM with comparison to the FEM. The temperature and normal flux on the boundary are approximated by the constant dual interpolation elements TS1 and QS1 in DiBFM, while these physical variables are approximated by quadratic tetrahedral elements in FEM. This problem is analyzed by the DiBFM with totally 2497, 3996, 6555 and 12176 source nodes, respectively. The reference solution is obtained by FEM with a very fine mesh of 9430007 nodes for comparison purposes. For example, the numerical results of DiBFM6555 and FEM9430007 are obtained by the DiBFM using 6555 source nodes and the FEM using 9430007 source nodes, respectively. Corresponding mesh generation of a cup by the DiBFM with totally 2497 the dual interpolation elements (including 1677 TS1 elements and 820 QS1 elements) is given in Fig. 21(b). As is shown in Fig. 22 and Fig. 23, the numerical results of the DiBFM with different source nodes are evaluated over 200 sample points uniformly distributed along a straight line AB on the bottom face of the cup. High accuracy can be obtained by the DiBFM with few source nodes. The temperature distribution in the whole domain is presented in Fig. 24.

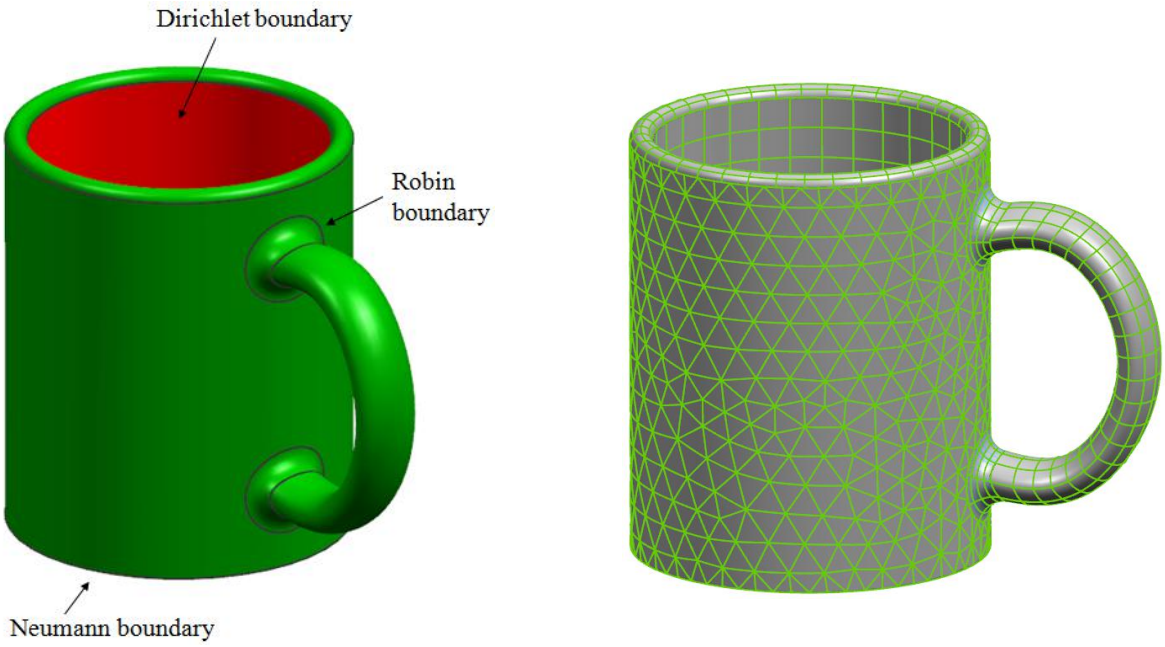

(a) Boundary conditions of the cup (b) Mesh generation of the cup

Fig. 21. Boundary conditions and mesh generation of the cup.

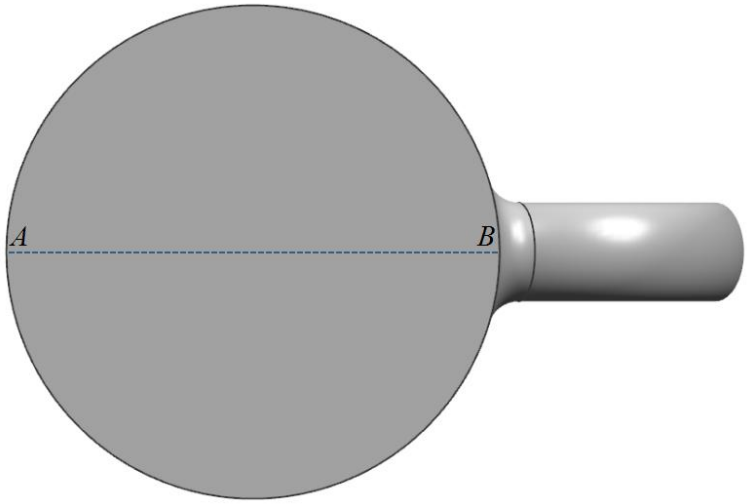

Fig. 22. Distribution of the sample points along a straight line AB for u .

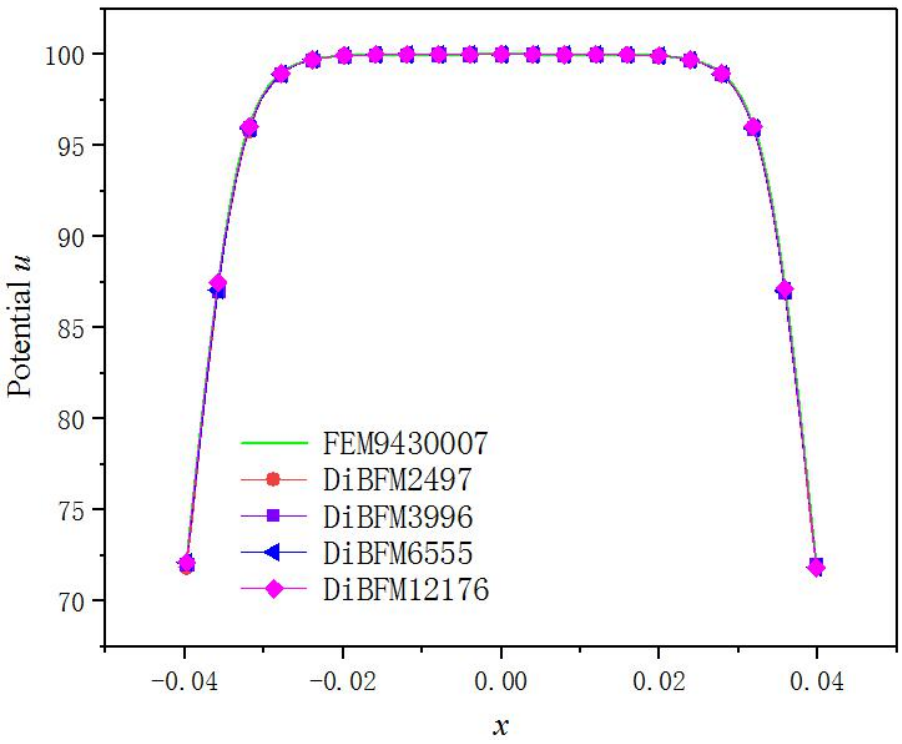

Fig. 23. The potential along the straight line AB.

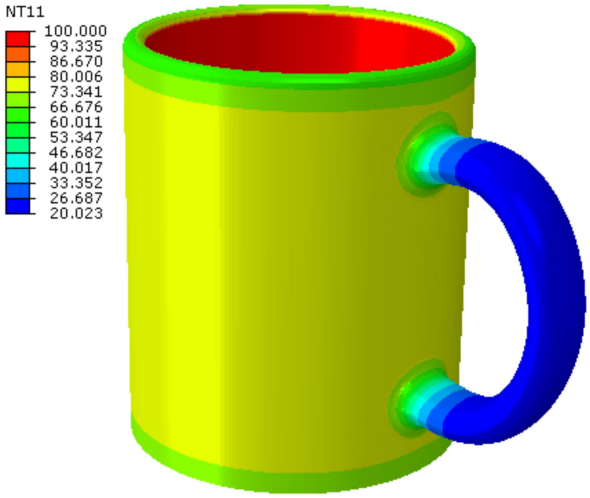

(a) The temperature u distribution of FEM in main view

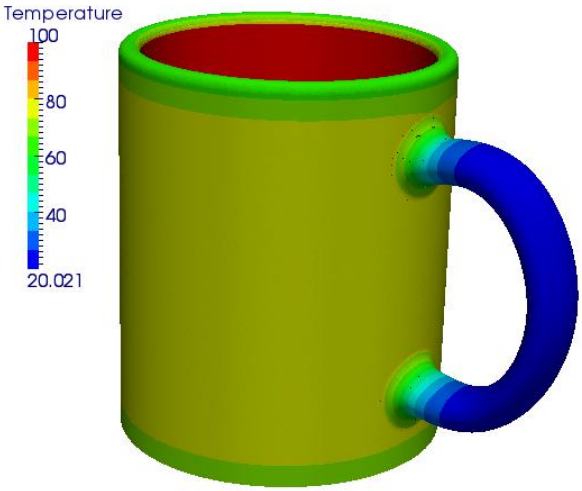

(b) The temperature u distribution of DiBFM in main view

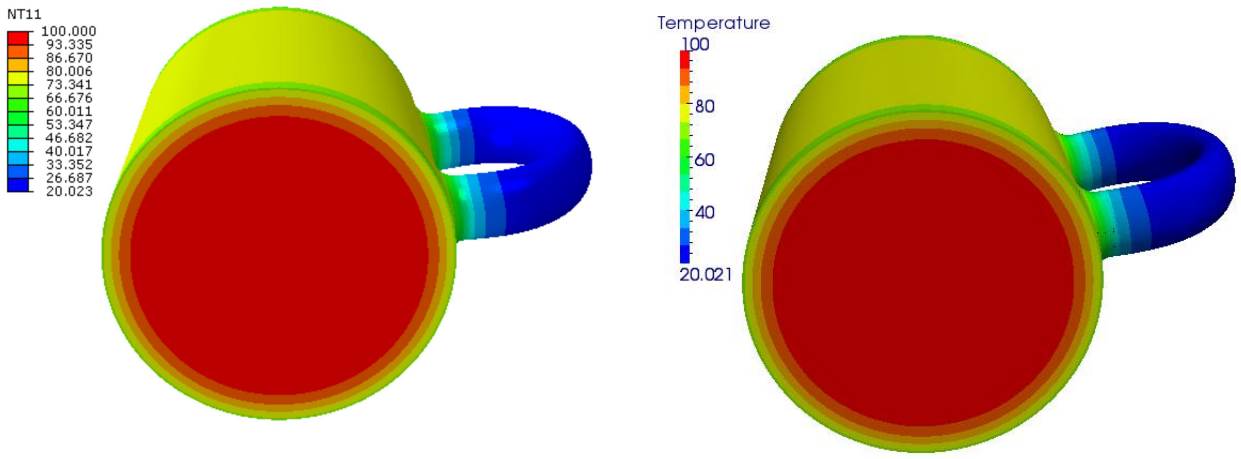

(c) The temperature u distribution of FEM on the bottom face outside the cup

(d) The temperature u distribution of DiBFM on the bottom face outside the cup

Fig. 24. The contour plots of temperature u in the whole domain: (a) (c) the reference solution obtained by FEM with 9430007 source nodes, (b) (d) DiBFM with 3996 source nodes.

We have demonstrated the potential of the DiBFM to handle complex, real world geometries in a fully automated manner, in the context of a geometric model of the cup. The CAD file of the cup was downloaded from the web. There was no alteration to it for the purposes of analysis, no feature removal and no geometry clean-up. In addition, meshing and analysis for complicated structures with complex geometries, such as the cup, are automatically executed without any manual operation [39]. The CAE analysis of the cup is implemented directly on the original CAD model rather than an elaborately built discretized model, which makes a truly seamless interaction between CAD and CAE successfully achieved.

From Fig. 23 and Fig. 24, results of the temperature obtained by the DiBFM with few source nodes are in good agreement with the reference solution. With the increasing number of all source nodes on the boundary of the cup, numerical results of the temperature obtained by the DiBFM and the FEM are both close to the reference solution. Obviously, it can be observed that the DiBFM can well deal with numerical analysis in complex geometries and can achieve a high level of accuracy.

6. Conclusions

A novel technique based on the dual interpolation boundary face method (DiBFM) has been proposed for three-dimensional potential problems. In this paper, a new type of elements named the dual interpolation elements are presented. A key advantage of the dual interpolation elements is that this type of elements can unify the continuous and discontinuous elements and improve the accuracy,

flexibility and convenience of the interpolation calculation. We have also introduced the construction of the dual interpolation functions for use with boundary integral equations in details. Even with some irregular elements in numerical simulation, accurate results and high convergence rates can be achieved by the DiBFM. In the DiBFM implementation, the geometric variables in the dual interpolation and the boundary integration are implemented directly on the bounding surfaces rather than an elaborately built discretized model, which makes a truly seamless interaction between CAD and CAE successfully achieved without any geometric simplification. Thus, the DiBFM could be an essential step in the process of automatic simulation based on this competitive advantage.

Numerical results are presented for several potential problems to demonstrate the validity, accuracy and convergence of the DiBFM. The DiBFM exhibits high accuracy and superior convergence behavior. It is flexible and convenient to handle complicated, real world geometries in a fully automated manner based on the DiBFM. Compared with the FEM, the results of the DiBFM with few source nodes are in good agreement with the reference solution. By combining with the fast multipole method [40,41], it can be applied into the specific domain of large-scale computations and high performance computing for complex structures. In future work, we plan on developing the DiBFM to solve 3-D problems through the use of discontinuous grids, which will substantially relieve the burden of mesh generation.

Conflict of interest

The authors declare that they have no conflict of interest.

Acknowledgements

This work was supported by National Science Foundation of China under grant number 11772125.

References

[1] J.H. Kane, Boundary Element Analysis in Engineering Continuum Mechanics, Prentice-Hall, Engelwood Cliffs, NJ, 1994.

[2] Qin X, J.M. Zhang, Liu L, et al. Steady-state heat conduction analysis of solids with small open-ended tubular holes by BFM[J]. International Journal of Heat and Mass Transfer, 2012, 55(23-24): 6846-6853.

[3] Zhou F, J.M. Zhang, Sheng X, et al. Shape variable radial basis function and its application in dual reciprocity boundary face method[J]. Engineering analysis with boundary elements, 2011, 35(2): 244-252.

[4] Zieniuk E. Potential problems with polygonal boundaries by a BEM with parametric linear functions[J]. Engineering Analysis with Boundary Elements, 2001, 25(3): 185-190.

[5] Zhou F, J.M. Zhang, Sheng X, et al. A dual reciprocity boundary face method for 3D non-homogeneous elasticity problems[J]. Engineering Analysis with Boundary Elements, 2012, 36(9): 1301-1310.

[6] A. Blázquez, F. Paris, Effect of numerical artificial corners appearing when using BEM on contact stresses, Eng. Anal. Bound. Elem. 35 (2011) 1029–1037.

[7] Oysu C. Finite element and boundary element contact stress analysis with remeshing technique. Applied Mathematical Modelling, 2007, 31(12): 2744-2753.

[8] Niu Z. R., Cheng C. Z, Ye J. Q, et al. A new boundary element approach of modeling singular stress fields of plane V-notch problems. International Journal of Solids and Structures, 2009, 46(16): 2999-3008.

[9] Dong C Y, Yang X, Pan E. Analysis of cracked transversely isotropic and inhomogeneous solids by a special BIE formulation [J]. Engineering analysis with boundary elements, 2011, 35(2): 200-206.

[10] Xie G, Zhou F, Zhang D, et al. A novel triangular boundary crack front element for 3D crack problems based on 8-node serendipity element[J]. Engineering Analysis with Boundary Elements, 2019, 105: 296-302.

[11] Peake M J, Trevelyan J, Coates G. Extended isogeometric boundary element method (XIBEM) for three-dimensional medium-wave acoustic scattering problems [J]. Computer Methods in Applied Mechanics and Engineering, 2015, 284: 762-780.

[12] X.H. Wang, J.M. Zhang, F.L. Zhou, An adaptive fast multipole boundary face method with higher order elements for acoustic problems in three-dimension, Eng. Anal. Bound. Elem. 37 (2013) 114–152.

[13] Zhang H, Zhao G, Ma X. Adaptive generation of hexahedral element mesh using an improved grid-based method. Computer-Aided Design, 2007, 39(10):914-928.

[14] Nguyen V P, Rabczuk T, Bordas S, et al. Meshless methods: a review and computer implementation aspects[J]. Mathematics and computers in simulation, 2008, 79(3): 763-813.

[15] J.M. Zhang, Yao Z, Li H. A hybrid boundary node method[J]. International Journal for Numerical Methods in Engineering, 2002, 53(4): 751-763.

[16] J.M. Zhang, Yao Z. Meshless regular hybrid boundary node method[J]. Computer Modeling in Engineering and Sciences, 2001, 2(3): 307-318.

[17] Hong Y, Lin J, Chen W. A typical backward substitution method for the simulation of Helmholtz problems in arbitrary 2D domains[J]. Engineering Analysis with Boundary Elements, 2018, 93: 167-176.

[18] Lin J, Zhang C, Sun L, et al. Simulation of seismic wave scattering by embedded cavities in an elastic half-plane using the novel singular boundary method[J]. Advances in Applied Mathematics and Mechanics, 2018, 10(2): 322-342.

[19] Hong Y, Lin J, Chen W. Simulation of thermal field in mass concrete structures with cooling pipes by the localized radial basis function collocation method[J]. International Journal of Heat and Mass Transfer, 2019, 129: 449-459.

[20] Vu-Bac N, Nguyen-Xuan H, Chen L, et al. A phantom-node method with edge-based strain smoothing for linear elastic fracture mechanics[J]. Journal of Applied Mathematics, 2013.

[21] Ong T H, Heaney C E, Lee C K, et al. On stability, convergence and accuracy of bES-FEM and bFS-FEM for nearly incompressible elasticity[J]. Computer Methods in Applied Mechanics and Engineering, 2015, 285: 315-345.

[22] Lee C K, Mihai L A, Hale J S, et al. Strain smoothing for compressible and nearly-incompressible finite elasticity[J]. Computers & Structures, 2017, 182: 540-555.

[23] Natarajan S, Bordas S P A, Ooi E T. Virtual and smoothed finite elements: a connection and its application to polygonal/polyhedral finite element methods[J]. International Journal for Numerical Methods in Engineering, 2015, 104(13): 1173-1199.

[24] Francis A, Ortiz - Bernardin A, Bordas S P A, et al. Linear smoothed polygonal and polyhedral finite elements[J]. International Journal for Numerical Methods in Engineering, 2017, 109(9): 1263-1288.

[25] Chakraborty S, Natarajan S, Singh S, et al. Optimal Numerical Integration Schemes for a Family of Polygonal Finite Elements with Schwarz–Christoffel Conformal Mapping[J]. International Journal for Computational Methods in Engineering Science and Mechanics, 2018, 19(4): 283-304.

[26] Atroshchenko E, Tomar S, Xu G, et al. Weakening the tight coupling between geometry and simulation in isogeometric analysis: From sub-and super-geometric analysis to Geometry-Independent Field approximaTion (GIFT)[J]. International Journal for Numerical Methods in Engineering, 2018, 114(10): 1131-1159.

[27] Li, C., Ooi, E. T., Song, C., & Natarajan, S. SBFEM for fracture analysis of piezoelectric composites under thermal load[J]. International Journal of Solids and Structures, 2015, 52: 114-129.

[28] Natarajan S, Wang J C, Song C, et al. Isogeometric analysis enhanced by the scaled boundary finite element method[J]. Computer Methods in Applied Mechanics and Engineering, 2015, 283: 733-762.

[29] W.F. Floreza, H. Powera, Comparison between continuous and discontinuous boundary elements in the multidomain dual reciprocity method for the solution of the two-dimensional Navier–Stokes equations, Eng. Anal. Bound. Elem. 25 (2001) 57-69.

[30] G.D. Manolis, P.K. Banerjee, Conforming versus non-conforming boundary elements in three-dimensional elastostatics, Internat. J. Numer. Methods Engrg, 23 (1986) 1885-1904.

[31] Rosen D, Cormack DE. On corner analysis in the BEM by the continuation approach. Eng Anal Bound Elem 1995;16:53–63.

[32] Guiggiani M, Krishnasamy G, Rudolphi TJ, Rizzo FJ. A general algorithm for the numerical solution of hypersingular boundary integral equations. J Appl Mech 1992;59:604–14.

[33] J.M. Zhang, W.C. Lin, Y.Q. Dong, A double-layer interpolation method for implementation of BEM analysis of problems in potential theory, Applied Mathematical Modelling, 51 (2017) 250-269.

[34] J.M. Zhang, X.Y. Qin, X. Han, A boundary face method for potential problems in three dimensions, Int. J. Numer. Methods Engrg. 80 (2009) 320-337.

[35] J.M. Zhang, W. Lin, Y. Dong, A dual interpolation boundary face method for elasticity problems, Eur. J. Mech. – A/Solids 73 (2019) 500–511.

[36] J.M. Zhang, Shu, X., Trevelyan, J., Lin, W., Chai, P. A solution approach for contact problems based on the dual interpolation boundary face method. Applied Mathematical Modelling, 70 (2019) 643-658.

[37] P. Lancaster, K. Salkauskas, Surface generated by moving least squares methods, Math. Comput. 37 (1981) 141–158.

[38] Frey P J , George P L . Mesh Generation: Application to Finite Elements[M]. ISTE, 2007.

[39] Scott M A, Simpson R N, Evans J A, et al. Isogeometric boundary element analysis using unstructured T-splines[J]. Computer Methods in Applied Mechanics and Engineering, 2013, 254: 197-221.

[40] Greengard L, Rokhlin V. A new version of the fast multipole method for the Laplace equation in three dimensions[J]. Acta numerica, 1997, 6: 229-269.

[41] J.M. Zhang, M. Tanaka, Fast HdBNM for large-scale thermal analysis of CNT-reinforced composites. Comput. Mech, 41 (2008) 777–787.